Investigation of the muon induced background at the KATRIN main spectrometer

Master's Thesis of

Johanna Linek

at the Department of Physics
Institute for Experimental Nuclear Physics

Reviewer:	Prof. Dr. Guido Drexlin
Second reviewer:	Prof. Dr. Thomas Müller
Advisor:	Dr. Florian Fränkle

01. June 2014 – 01. June 2015

I declare that I have developed and written the enclosed thesis completely by myself, and have not used sources or means without declaration in the text.

Karlsruhe, 01.06.2015

. . . .

(Johanna Linek)

Abstract

The very challenging investigations of neutrino properties and particularly their mass is of major interest in particle physics and cosmology. The discovery of neutrino oscillations implied that neutrinos are massive particles, however neutrino oscillations are only sensitive to the differences between the squared neutrino mass eigenstates and therefore only a lower limit of 0.049 eV/c^2 on the heaviest mass eigenstate was obtained [73]. Direct measurements investigating the kinematics of β-decays on the other hand were able to set an upper limit of 2 eV/c^2 on the effective mass $m_{\bar{\nu}_e}$ of the electron antineutrino. The ambitious goal of the **KA**rlsruhe **TRI**tium **N**eutrino (KATRIN) experiment is to determine $m_{\bar{\nu}_e}$ with a sensitivity of 200 meV/c^2. This will be achieved by precisely scanning the endpoint region of the electron energy spectrum of tritium β-decay ($\approx$ 18.6 keV) using a high-resolution spectrometer system of MAC-E type.

In order to reach such a high sensitivity, a low background rate of 0.01 counts per second (cps) is required. It is expected that a major background component is due to cosmic muon induced secondary electrons from the large inner surface area of the KATRIN main spectrometer. In order to allow for detailed investigations of this background component, a scintillator based muon detection system was installed in close proximity of the main spectrometer. As the muon rate shows fluctuations in time, a corresponding variation of the background electron rate is expected if those electrons are muon induced. This thesis focuses on the investigation of the muon induced background using those variations for correlation studies.

For an investigation of the cosmic muon flux variations, the muon detector system was continuously operated in a standalone mode for three months. Relative fluctuations of up to ± 3.5 % have been observed. The muon rate variations and its dependence on atmospheric parameters have been studied. A correlation between the muon rate and the atmospheric pressure of $r = -0.64$ has been found. Diurnal variations of the muon flux originating in a spatial anisotropy of the primary cosmic ray flux were observed.

In order to investigate the correlation between cosmic muons passing through the main spectrometer and background electrons reaching the detector, a longterm background measurement with parallel operation of main spectrometer and the muon detector system was performed as an important part of the second SDS[1] commissioning phase. Three different electromagnetic configurations of the SDS system, which were alternated periodically over the course of the measurement, were chosen to investigate different aspects of the muon induced background.

Within the scope of this thesis, an analysis strategy has been developed for detailed

[1] **S**pectrometer and **D**etector **S**ection

correlation studies with the goal to determine the influence of cosmic muons on the background at the KATRIN main spectrometer. As a major result of these correlation studies it can be stated that only about 15 % of the secondary electrons at the inner surface of the spectrometer are induced by cosmic muons. The spectrometer background with active magnetic and electrostatic shielding shows no significant correlation with the muon flux variations, therefore it can be concluded that the spectrometer background is dominated by background processes not induced by cosmic muons.

Zusammenfassung

Untersuchungen von Neutrinoeigenschaften im Allgemeinen und ihrer Masse im Speziellen sind einerseits eine große Herausforderung, andererseits aber auch von besonderem Interesse für die Teilchenphysik und Kosmologie. Die Entdeckung der Neutrino Oszillationen hat gezeigt, dass Neutrinos eine Masse haben, allerdings sind diese Experimente nur auf die Differenz der quadrierten Masseneigenzustände der Neutrinos sensitiv, weshalb durch sie nur ein unteres Limit von $0,049\,\mathrm{eV/c^2}$ auf den schwersten Masseneigenzustand erlangt werden konnte [73]. Direkte Messungen hingegen, die die Kinematik von β-Zerfällen untersuchen, konnten ein oberes Limit von $2\,\mathrm{eV/c^2}$ auf die effektive Masse des Elektron-Antineutrinos festsetzen. Das ehrgeizige Ziel des **K**arlsruhe **TRI**tium **N**eutrino Experiments (KATRIN) ist die Bestimmung von $m_{\bar{\nu}_e}$ mit einer Sensitivität von $200\,\mathrm{meV/c^2}$. Dazu wird ein hochauflösendes Spektrometersystem vom Typ MAC-E-Filter verwendet, um das Energiespektrum der Elektronen im Bereich nahe des Endpunkts ($18,6\,\mathrm{keV}$) mit hoher Präzision zu vermessen.

Um solch eine hohe Sensitivität zu erreichen, wird eine geringe Untergrundrate von $0,01$ Ereignissen pro Sekunde benötigt. Den Erwartungen zufolge besteht ein großer Teil des Untergrunds aus myoninduzierten Sekundärelektronen, die von der großen inneren Oberfläche des KATRIN Hauptspektrometers emittiert werden. Um detaillierte Untersuchungen dieser Untergrundkomponente zu ermöglichen, wurde ein Myondetektorsystem aus Szintillatormodulen in der Nähe des Hauptspektrometers installiert. Da die Myonenrate zeitliche Fluktuationen aufweist, wird eine entsprechende Variation der Untergrundrate an Elektronen erwartet, sofern diese von kosmischen Myonen verursacht werden. Der Schwerpunkt dieser Arbeit liegt auf der Untersuchung des myoninduzierten Untergrunds, wobei die Fluktuationen für Korrelationsanalysen genutzt werden.

Zur Untersuchung der Variationen der kosmischen Myonenrate wurde das Myondetektorsystem drei Monate lang durchgehend in einem autonomen Modus betrieben. In dieser Messung wurden relative Fluktuationen von bis zu $\pm 3,5\,\%$ beobachtet. Die Variationen in der Myonenrate und ihre Abhängigkeit von atmosphärischen Parametern wurde untersucht. Dabei wurde eine Korrelation von $r = -0,64$ zwischen der Myonenrate und dem Atmosphärendruck gefunden. Tageszeitliche Variationen des Myonenflusses, die ihren Ursprung in einer räumlichen Anisotropie des Flusses der primären kosmischen Strahlung haben, wurden ebenfalls beobachtet.

Um die Korrelation zwischen kosmischen Myonen, die das Spektrometer durchqueren, und Untergrundelektronen, die am Detektor gemessen werden, untersuchen zu können, wurde eine Langzeitmessung durchgeführt, in der das Hauptspektrometer und das Myondetektorsystem parallel betrieben wurden. Diese Messung war ein wichtiger Bestandteil

der zweiten SDS[2] Inbetriebnahmephase. Um verschiedene Aspekte des myoninduzierten Untergrunds zu untersuchen, wurden drei verschiedene elektromagnetische Konfigurationen des SDS-Systems ausgewählt, die über die gesamte Messzeit periodisch wiederholt wurden.

Im Rahmen dieser Arbeit wurde eine Strategie zu einer detaillierten Korrelationsanalyse entwickelt mit dem Ziel, den Einfluss des myoninduzierten Untergrunds am KATRIN Hauptspektrometer zu bestimmen. Eines der Hauptresultate dieser Korrelationsstudien ist, dass nur ca. 15 % der Sekundärelektronen an der inneren Oberfläche des Spektrometers durch kosmische Myonen verursacht wird. Der Spektrometeruntergrund mit aktiver magnetischer und elektrostatischer Abschirmung zeigt keine signifikante Korrelation mit den Variationen im Myonenfluss, woraus geschlossen werden kann, dass der Spektrometeruntergrund von anderen Untergrundprozessen dominiert ist, die nicht durch kosmische Myonen verursacht werden.

[2]**S**pectrometer and **D**etector **S**ection

Contents

1. Neutrino physics

Neutrino physics is a fascinating field with many important unanswered questions. For instance: Are there more than three neutrino flavors, are neutrinos Dirac or Majorana particles or what is the absolute mass scale of neutrinos? Neutrinos interact only very weakly and therefore escape most attempts to investigate their properties. In this chapter an overview of previous successes in those attempts (sections 1.1, 1.2), current experiments and future plans (sections 1.3, 1.4) will be given.

1.1. Historical Overview

When J. Chadwick measured the energy spectrum of electrons emitted in radium β-decay in 1914, he discovered against all expectations that it was a continuous spectrum [1]. Assuming a two-body-decay this was not possible without breaking conservation of energy, momentum and angular momentum. One possible solution to preserve these conservation laws was given by W. Pauli in 1930 [2], when he postulated a neutral spin-$^1/_2$ particle later called the neutrino. In the β^--decay of a parent nucleus X with A nucleons (Z protons, $A-Z$ neutrons) into the daughter nucleus Y

$$^{A}_{Z}\mathrm{X} \rightarrow \, ^{A}_{Z+1}\mathrm{Y} + \mathrm{e}^- + \overline{\nu}_\mathrm{e} \tag{1.1}$$

an electron and an antineutrino are emitted. The underlying process is a neutron decaying into a proton

$$\mathrm{n} \rightarrow \mathrm{p} + \mathrm{e}^- + \overline{\nu}_\mathrm{e}. \tag{1.2}$$

It was not until 1956 that Pauli's theory got confirmed with the discovery of the neutrino by F. Reines and C. Cowan [3]. At that time nuclear reactors were the strongest neutrino sources available. Electron antineutrinos originating from the reactor have been detected via the following reaction

$$\overline{\nu}_\mathrm{e} + \mathrm{p} \rightarrow \mathrm{e}^+ + \mathrm{n}. \tag{1.3}$$

The detector basically consisted of a $CdCl_2$ loaded water tank surrounded by liquid scintillators. After reaction (1.3), the positron quickly loses its kinetic energy and annihilates with an electron producing two monochromatic photons with an energy of $E_\gamma = 511\,\mathrm{keV}$ each, which gives the first prompt signal. The neutron on the other hand gets slowly moderated by collisions with hydrogen atoms before it is captured by a cadmium nucleus leaving it in an excited state. A second signal is then provided by photon emission of the cadmium nucleus as it deexcites to the ground state. Therefore the signature for reaction (1.3) consists of two photon signals separated by several µs. This delayed coincidence method finally lead to the first discovery of the neutrino.

The proof that there is more than just one flavor of neutrinos was given in 1962 by L. Lederman, M. Schwartz and J. Steinberger when they discovered the muon neutrino [4]. They used the Alternating Gradient Synchrotron (AGS) in Brookhaven where 15 GeV protons were shot towards a beryllium target producing pions which decay mainly via

$$\pi^{\pm} \rightarrow \mu^{\pm} + \overset{(-)}{\nu}. \tag{1.4}$$

In a distance of 21 m behind the target was a 13.5 m thick iron wall, absorbing everything but the neutrinos. Further downstream was a spark chamber, where the neutrinos could be detected.

With the discovery of the tau lepton in 1975 at the Stanford Linear Accelerator (SLAC) also a third neutrino was expected to exist. Nevertheless it took another 25 years before the DONUT Collaboration finally announced the discovery of the tau neutrino in 2000 [5]. The experiment was located at Fermilab, where the Tevatron was used to create a neutrino beam by shooting protons onto a tungsten target. The ν_τ's originated mainly from charmed mesons decaying leptonically. As target they used a combination of steel sheets with emulsion plates. An incoming tau neutrino produces a tau lepton in the steel, which then decays after a few mm with the typical signature of a kink in its trajectory.

1.2. Properties of the standard model neutrino

The Standard Model of particle physics is a well established collection of knowledge over the most elementary particles in the universe. It correctly describes many properties of matter and antimatter very accurately and gives an explanation to many experimental results, but it also has its weaknesses and eventually some enhancements will be necessary. An overview of the Standard Model can be seen in Figure 1.1. There are 12 fermions which can be split into three generations, each containing two quarks and two leptons, and their antiparticles. The fourth column contains the gauge bosons representing the strong, weak and electromagnetic interactions. Only recently, the last particle in the Standard Model, the Higgs boson, has been discovered at the Large Hadron Collider (LHC) at CERN in 2012 [6, 7].

The fact that neutrinos only participate in weak interactions makes it very difficult to investigate their properties. Neutrinos are neutral spin-$^1\!/_2$ particles and in the simple case of the Standard Model considered massless. With direct neutrino measurements through kinematic analyses of weak interactions, so far only an upper limit of 2 eV/c^2 [8, 9] could be determined for the mass of the neutrinos. But as will be seen in section 1.3, there is another measurable effect that requires neutrinos to have nonzero mass.

As the mediators of the weak interaction only couple to left-handed fermions and right-handed antifermions, only left-handed neutrinos and right-handed antineutrinos have been observed. There is a theory though, that right-handed neutrinos or left-handed antineutrinos may exist. These particles would not take part in the usual interactions and are therefore called sterile neutrinos.

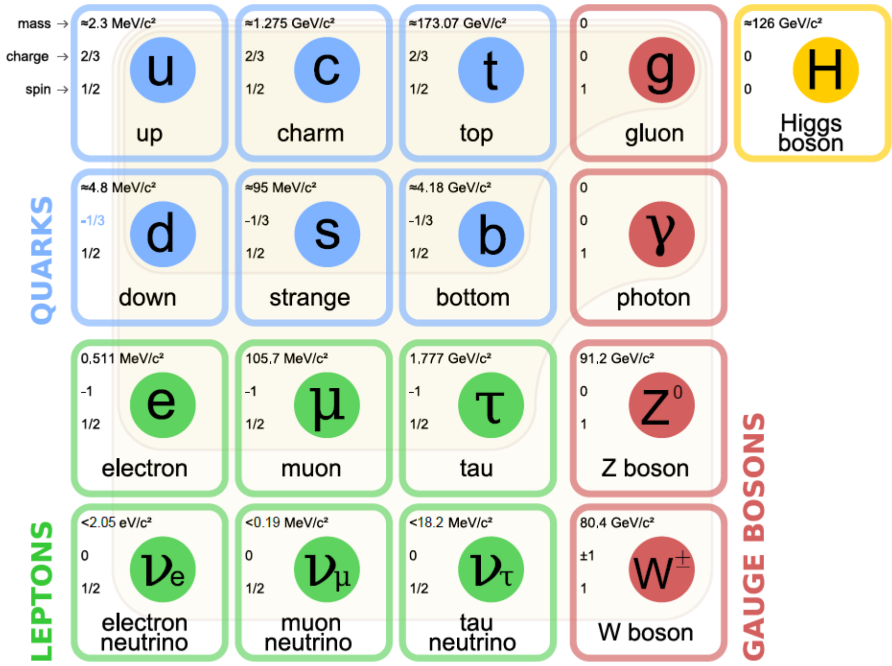

Figure 1.1.: Overview over all elementary particles in the Standard Model and some of their properties. In the first three columns are the three generations of quarks and leptons, the fourth column shows the gauge bosons representing their interactions and in the fifth column is the Higgs boson. Figure taken from [10].

1.3. Neutrino oscillations

The idea of neutrino oscillations was first proposed by B. Pontecorvo in 1957 [11, 12]. He suggested that neutrinos could perform oscillations similar to those of neutral kaons due to $\mathrm{K}^0 \leftrightarrow \bar{\mathrm{K}}^0$ mixing. While most physicists at that time still believed in massless neutrinos, with this theory Pontecorvo already anticipated massive neutrinos and the violation of lepton number conservation.

1.3.1. The solar neutrino problem

Neutrino sources can be split into two groups: There are artificial sources like nuclear reactors and accelerators and natural sources like supernovae and their remnants, the Earth's atmosphere and the Sun. Investigations of the latter lead to the so called solar neutrino problem casting doubt on the standard solar model (SSM). In the SSM [13] there are several different processes that lead to the production of ν_e, the most dominant one being the pp-chain reaction:

$$2\mathrm{e}^- + 4\mathrm{p} \longrightarrow {}^4\mathrm{He} + 2\nu_e + 26.73\,\mathrm{MeV}. \tag{1.5}$$

The whole energy spectrum of the solar neutrino flux at Earth expected from the SSM can be seen in Figure 1.2. From the late 60s on there have been several experiments measuring the solar neutrino flux, the Homestake Experiment by R. Davis and J. Bahcall [14] being

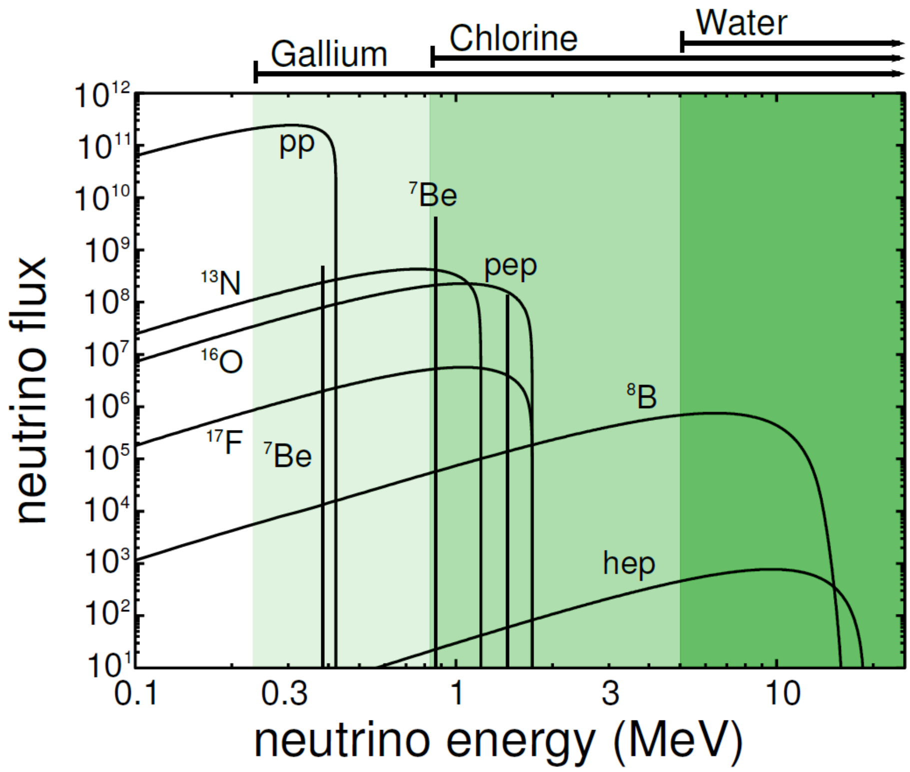

Figure 1.2.: Spectrum of the solar neutrino flux in the standard solar model. The target materials used for the different chains are indicated by the shaded areas. Figure adapted from [17]

the first one to observe a deficit of electron neutrinos compared to the theoretical flux expected from the SSM.

In 2001 the solar neutrino problem finally got resolved by the Sudbury Neutrino Observatory (SNO) experiment [15]. The detector consisted of a 1000 t heavy water Cherenkov tank surrounded by approximately 9500 photomultipliers. They measured ^{8}B neutrinos according to the following interactions:

$$\begin{array}{lrcl} \text{Charged Current:} & \nu_e + d & \rightarrow & p + p + e^- \\ \text{Neutral Current:} & \nu_\alpha + d & \rightarrow & p + n + \nu_\alpha \\ \text{Elastic scattering:} & \nu_\alpha + e^- & \rightarrow & \nu_\alpha + e^- \end{array} \tag{1.6}$$

where $\alpha = e, \mu, \tau$. They discovered that the total neutrino flux was consistent with the expected one, confirming the theory, that on their way from the core of the Sun to the Earth, some of the electron neutrinos change their flavor and become muon or tau neutrinos.

The first detection of solar pp-neutrinos by the Borexino collaboration [16] is a further confirmation of the validity of the SSM. Their detector consists of a 278 t ultrapure liquid scintillator inside a spherical vessel surrounded by over 2000 PMTs and is located deep underground in the Gran Sasso laboratory in Italy. The Borexino detector is able to measure all neutrino flavors via elastic neutrino-electron scattering. The key to their success was the achievement of a very low radioactive background inside the detector volume.

1.3.2. Theoretical description

The basic concept of neutrino oscillations relies on the fact, that neutrino mass eigenstates $|\nu_i\rangle$ $(i = 1,2,3)$ are not identical to their flavor eigenstates $|\nu_\alpha\rangle$ $(\alpha = \mathrm{e},\mu,\tau)$. Maki, Nakagawa and Sakata introduced the PMNS[1] matrix U [18] in analogy to the quark mixing matrix to relate those two different sets of eigenstates:

$$|\nu_\alpha\rangle = \sum_i U_{\alpha,i}\,|\nu_i\rangle. \tag{1.7}$$

By introducing three mixing angles $\theta_{12}, \theta_{23}, \theta_{13}$ and a CP violating phase δ as parametrization, the unitary matrix U can be split into three separate parts. Also taking into account the possibility that neutrinos are Majorana particles, i.e. that they are identical to their own antiparticles, two additional phase parameters α_1 and α_2 have to be added as well:

$$U = \begin{pmatrix} 1 & 0 & 0 \\ 0 & c_{23} & s_{23} \\ 0 & -s_{23} & c_{23} \end{pmatrix} \cdot \begin{pmatrix} c_{13} & 0 & s_{13}e^{-i\delta} \\ 0 & 1 & 0 \\ -s_{13}e^{-i\delta} & 0 & c_{13} \end{pmatrix} \cdot \begin{pmatrix} c_{12} & s_{12} & 0 \\ -s_{12} & c_{12} & 0 \\ 0 & 0 & 1 \end{pmatrix} \cdot \begin{pmatrix} 1 & 0 & 0 \\ 0 & e^{i\alpha_1/2} & 0 \\ 0 & 0 & e^{i\alpha_2/2} \end{pmatrix} \tag{1.8}$$

where $c_{ij} = \cos\theta_{ij}$ and $s_{ij} = \sin\theta_{ij}$.
At the time of its production $(t = 0)$, the neutrino is in a pure flavor eigenstate, whereas for its propagation the mass eigenstates become important. The time dependence of the mass eigenstates can be written as

$$|\nu_i(t)\rangle = e^{-iE_i t}\,|\nu_i\rangle\,. \tag{1.9}$$

Hence

$$|\nu_\alpha(t)\rangle = \sum_i U_{\alpha i} e^{-iE_i t}\,|\nu_i\rangle = \sum_{i,\beta} U_{\alpha i} U^*_{\beta i} e^{-iE_i t}\,|\nu_\beta\rangle\,, \tag{1.10}$$

where the stationary mass eigenstates have been replaced by a superposition of flavor eigenstates. Using Equation 1.10, the probability for a neutrino of one flavor ν_α to transition into a neutrino of different flavor ν_β can be calculated as follows [19]:

$$P_{\nu_\alpha\to\nu_\beta}(t) = \left|\langle\nu_\beta(t)|\nu_\alpha(t)\rangle\right|^2 = \left|\sum_i U^*_{\alpha i} e^{-iE_i t} U_{\beta i}\right|^2 = \sum_{i,j} U^*_{\alpha i} U_{\beta i} U_{\alpha j} U^*_{\beta j} e^{-i(E_i - E_j)t}. \tag{1.11}$$

In the ultra-relativistic limit $(p_i = p = E)$ the transition probability becomes:

$$P_{\nu_\alpha\to\nu_\beta}(L/E) = \sum_{i,j} U^*_{\alpha i} U_{\beta i} U_{\alpha j} U^*_{\beta j} e^{-i\frac{\Delta m^2_{ij} L}{2E}}\,. \tag{1.12}$$

Here, L is the distance between the source and the detector, E corresponds to the energy of the neutrino and $\Delta m^2_{ij} \equiv m_i^2 - m_j^2$ are the mass splitting terms representing the phase of the oscillation. That way the oscillations can be described in terms of appearance and disappearance probabilities of different flavors.

[1]The P stands for Pontecorvo as he provided the idea of neutrino mixing, although in some literature it is just the MNS matrix

1.3.3. Experiments

The first experiment to prove the concept of neutrino oscillations was Super-Kamiokande in 1998 [20]. Super-Kamiokande is a 50 kt water Cherenkov detector with more than 11000 photomultipliers located in the Kamioka mine in Japan. An important feature of the detector is that it can distinguish between ν_e and ν_μ induced events. Analyses of atmospheric neutrinos showed a significant deficit of muon neutrinos that was consistent with a two-neutrino flavor oscillation between ν_μ and ν_τ. The oscillation probability in this case is a function of the zenith angle, as downward going neutrinos only traveled about 15 km and upward going neutrinos traveled about 13 000 km before reaching the detector. This results in a variation of the ratio $r = \nu_\mu / \nu_e$ for different zenith angles.

Another way to measure the parameters for $\nu_\mu \leftrightarrow \nu_\tau$ oscillations are long baseline accelerator experiments. In these experiments, an accelerator is used to create a muon neutrino beam, whereas in a detector several hundreds of kilometers away the disappearance probability into tau neutrinos is measured. Examples for such experiments are CNGS [21], MINOS [22] and K2K [23].

For solar neutrino experiments, which are used to investigate $\nu_e \leftrightarrow \nu_\mu$ oscillations, there are two different detection techniques. One is a radiochemical approach used for example in the Homestake experiment [14], where a 600 t tank with liquid C_2Cl_4 has been exposed to the solar neutrino flux for several weeks. The neutrinos transformed some of the chlorine into argon according to

$$\nu_e + {}^{37}\mathrm{Cl} \rightarrow {}^{37}\mathrm{Ar} + \mathrm{e}^-. \tag{1.13}$$

The argon atoms were then extracted and counted radiochemically. Similar to that, GALLEX [24], SAGE [25] and GNO [26] used the transformation of ^{71}Ga into ^{71}Ge to do the same. The other technique is represented by so called real-time experiments like Super-Kamiokande and SNO, which were both already described above.

Last but not least, neutrinos from nuclear reactors can be used to investigate $\nu_e \leftrightarrow \nu_\mu$ oscillations in long baseline experiments (KamLAND [27]) and $\nu_e \leftrightarrow \nu_\tau$ oscillations in short baseline experiments such as Daya Bay [28], Double Chooz [29] and RENO [30].

1.4. Determination of the neutrino mass

Investigations of neutrino oscillations have made it very clear, that neutrinos have a mass, but they are not able to determine the absolute neutrino masses. For that there are basically two types of measurements: model independent investigations of the kinematics of single β-decay (subsection 1.4.1) and model dependent methods like the neutrinoless double beta decay (subsection 1.4.2) or various cosmological methods which will not be discussed within this thesis.

1.4.1. Single β-decay

At present, the most promising way to determine the mass of the electron antineutrino is to investigate the β^--decay of tritium via a precise measurement of the electron energy

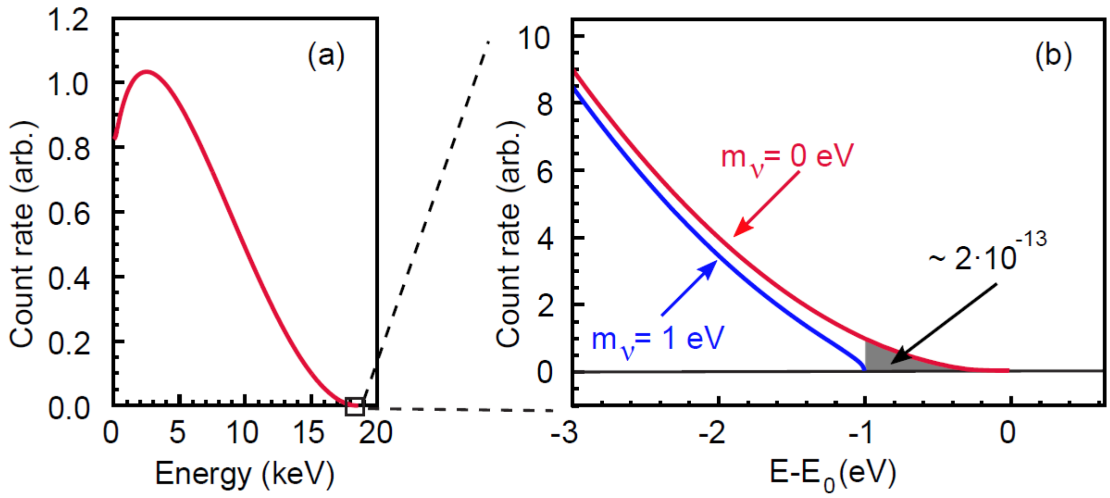

Figure 1.3.: a) Electron energy spectrum of the tritium beta decay. **b)** Zoom into the endpoint region for $m_{\nu_e} = 0\,\text{eV}$ and $m_{\nu_e} = 1\,\text{eV}$. Figure taken from [31].

spectrum at the endpoint. The KATRIN experiment will use this approach, therefore it will be described here in more detail. Tritium has been chosen for several reasons, two of them being its relatively low endpoint energy of about 18.6 keV and its high specific activity of $3.6{\cdot}10^{14}$ Bq/g.

Tritium decays into helium via

$$^3\text{H} \rightarrow \, ^3\text{He} + \text{e}^- + \overline{\nu}_\text{e}, \tag{1.14}$$

where the underlying process is the decay of a neutron into a proton (see Equation 1.2). By applying Fermi's Golden Rule, the following formula for the electron energy spectrum can be derived [32]:

$$\frac{\text{d}^2N}{\text{d}E\text{d}t} = \frac{G_F^2 \cos^2\theta_C}{2\pi^3 c^5 \hbar^7} \cdot |M|^2 \cdot F(E, Z+1) \cdot p_\text{e} \cdot \left(m_\text{e}c^2 + E\right) \cdot (E_0 - E) \cdot \sqrt{(E_0 - E)^2 - m_{\nu_\text{e}}^2 c^4}, \tag{1.15}$$

where G_F is the Fermi coupling constant, θ_C the Cabibbo angle, M the hadronic matrix element, $F(E, Z+1)$ the Fermi function, p_e, m_e and E are the momentum, mass and energy of the electron and E_0 is the endpoint energy in case of massless neutrinos. The free parameter here is the squared electron neutrino mass, which is actually – due to the neutrino mixing introduced in the last section – a weighted average of the mass eigenstates

$$m_{\nu_\text{e}}^2 = \sum_{i=1}^{3} |U_{\text{e}i}|^2 \cdot m_{\nu_i}^2. \tag{1.16}$$

The electron energy spectrum for tritium β-decay is shown in Figure 1.3, with a zoom in the endpoint region in b). A deviation can be seen for nonzero neutrino mass leading to a deformation of the spectrum and a lower endpoint energy. Results of previous measurements of the electron antineutrino mass are shown in Figure 1.4.

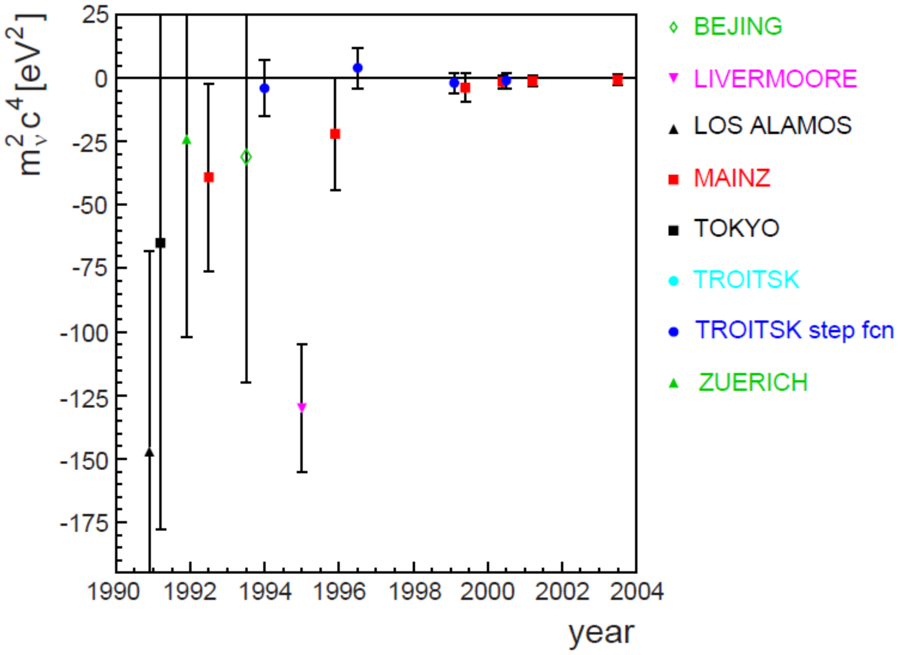

Figure 1.4.: Results of neutrino mass measurements from the past 25 years. Currently the best limit is $m_{\nu_e} < 2\,\mathrm{eV/c^2}$ by the Mainz and Troitsk experiments [8, 9]. Figure taken from [31].

It should be mentioned, that the identity of the electron neutrino mass to the electron antineutrino mass is only true for CPT invariance. Other experiments such as ECHo [33] want to test that assumption by a direct measurement of the electron neutrino mass. Furthermore, a new type of measurement for the electron energy spectrum from β-decays through a detection of coherent cyclotron radiation has been developed by the Project 8 collaboration [34].

1.4.2. Neutrinoless double beta-decay

Ordinary double β-decay ($2\nu\beta\beta$) can occur, if the single β-decay is energetically forbidden. In this very rare decay, two electrons or positrons and two neutrinos are emitted:

$$\begin{aligned} &2\mathrm{p} \rightarrow 2\mathrm{n} + 2\mathrm{e}^+ + 2\nu_\mathrm{e} \qquad (2\nu\beta^+\beta^+) \\ &2\mathrm{n} \rightarrow 2\mathrm{p} + 2\mathrm{e}^- + 2\overline{\nu}_\mathrm{e} \qquad (2\nu\beta^-\beta^-) \end{aligned} \tag{1.17}$$

Thus the energy spectrum is continuous, as can be seen in Figure 1.5b. This decay has been observed for several isotopes already, all with a half life of more than 10^{18} years.

E. Majorana developed a theory in 1937, where the neutrino is identical to its own antiparticle [37]. With this so called Majorana neutrino the double β-decay could also occur without the emission of two ν's. The corresponding Feynman graph is shown in Figure 1.5a. Such a decay would show up as a single peak in the electron energy spectrum (Figure 1.5b) but so far it has not been observed. There are several experiments looking for the neutrinoless

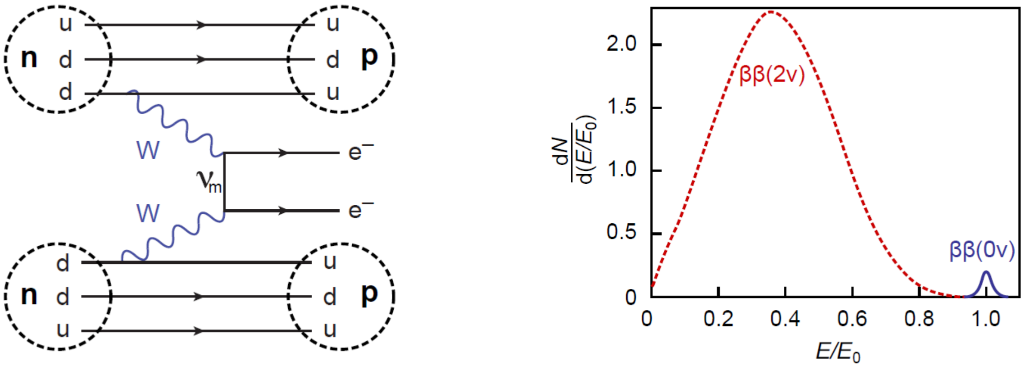

Figure 1.5.: a) Feynman diagram for the neutrinoless double beta decay. Figure taken from [35]. **b)** Continuous spectrum of the two electrons from $2\nu\beta\beta$-decay normalized to 1 (red) and $0\nu\beta\beta$ peak normalized to 10^{-2} (blue), both for a detector resolution of 5 % [36].

double beta decay, for example GERDA [38], CUORE [39] or MAJORANA [40].

These experiments measure the half life $T_{1/2}^{0\nu\beta\beta}$, which is connected to the effective Majorana neutrino mass $m_{\mathrm{ee}} = \left|\sum_{i=1}^{3} U_{\mathrm{e}i}^2 \cdot m_i\right|$ via

$$\left(T_{1/2}^{0\nu\beta\beta}\right)^{-1} = G^{0\nu\beta\beta}(Q_{\beta\beta}, Z) \cdot \left| M_{\mathrm{GT}}^{0\nu\beta\beta} - \left(\frac{g_{\mathrm{V}}}{g_{\mathrm{A}}}\right)^2 M_{\mathrm{F}}^{0\nu\beta\beta} \right|^2 \cdot \frac{\langle m_{\mathrm{ee}} \rangle}{m_{\mathrm{e}}^2} \tag{1.18}$$

with the phase space factor $G^{0\nu\beta\beta}$, endpoint energy $Q_{\beta\beta}$, atomic number Z, the Gamov-Teller $M_{\mathrm{GT}}^{0\nu\beta\beta}$ and Fermi $M_{\mathrm{F}}^{0\nu\beta\beta}$ matrix elements, the axial g_{A} and vector g_{V} coupling constants and the electron mass m_{e}. A discovery of the $0\nu\beta\beta$-decay would yield the neutrino mass and answer the question whether the neutrino is a Dirac or a Majorana particle, but more importantly it would also provide evidence for lepton number violation.

2. The KATRIN experiment

The **KA**rlsruhe **TRI**tium **N**eutrino experiment (KATRIN) aims to measure the electron antineutrino mass with a sensitivity of 200 meV/c^2 (90 % C.L.). It is currently under construction at the Karlsruhe Institute of Technology in Germany and scheduled to start measurements in 2016. An overview of the KATRIN setup can be seen in Figure 2.1. Electrons being produced in tritium β-decay at the WGTS[1] (section 2.1), travel through the transport section (section 2.2), are energetically selected by two MAC-E filter[2] type spectrometers (section 2.3) before the most energetic electrons with an energy near the endpoint E_0 reach the detector (section 2.4). The main background sources relevant for KATRIN will be discussed in section 2.5.

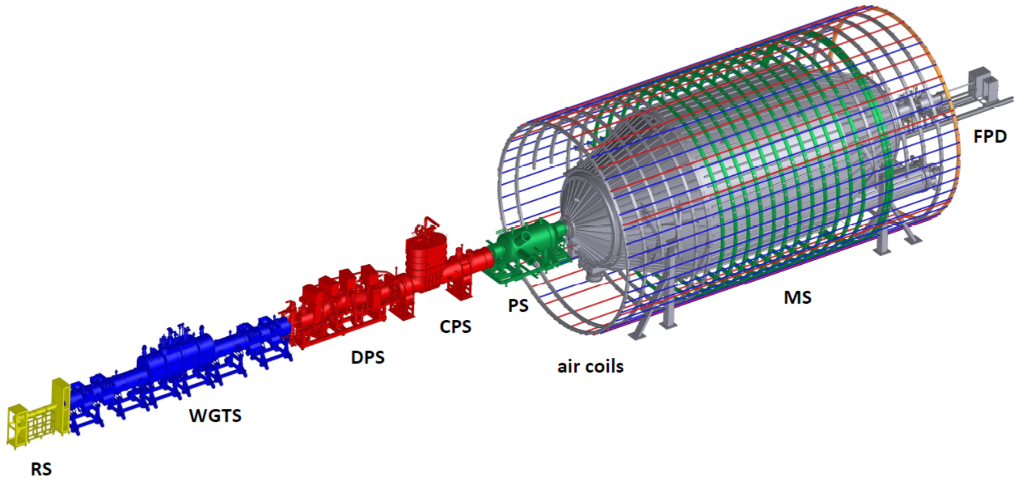

Figure 2.1.: Overview of the KATRIN components: The rear section (RS) and the windowless gaseous tritium source (WGTS), followed by the transport section consisting of the differential (DPS) and cryogenic (CPS) pumping section, the pre-spectrometer (PS) and the main spectrometer (MS) and the focal plane detector system (FPD). The whole setup is about 70 m long. Figure taken from [46].

2.1. WGTS and rear section

The windowless gaseous tritium source (WGTS) [44] consists of a 10 m long cylindric tube with a diameter of 9 cm (see Figure 2.2), which is cooled to 30 K by a two phase neon cooling system [45]. The tritium molecules T_2 are injected in the middle of the beam tube

[1]**W**indowless **G**aseous **T**ritium **S**ource

[2]**M**agnetic **A**diabatic **C**ollimation combined with an **E**lectrostatic filter [41–43]

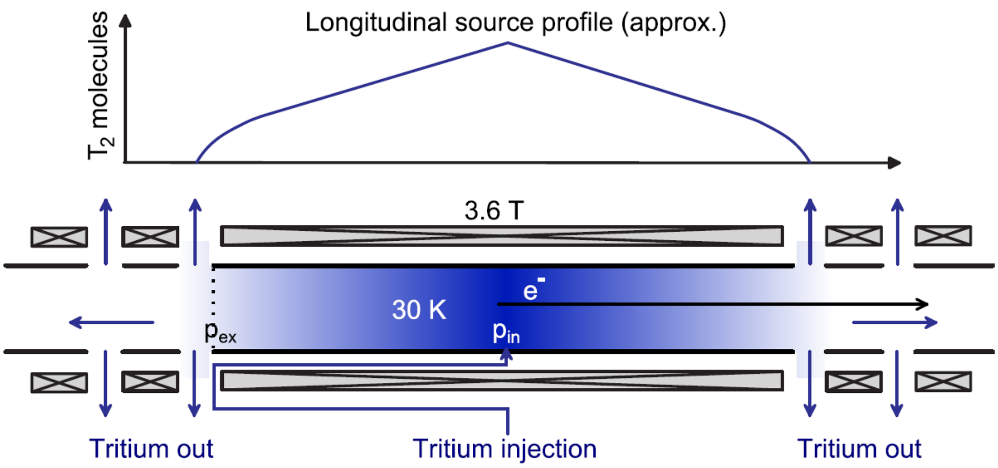

Figure 2.2.: Schematic view of the WGTS including a visualization of the column density profile of the tritium molecules in the beam tube. Figure taken from [44].

from where they diffuse to both ends. They are then pumped out and reinjected after passing through the Inner Loop, in which contaminants are removed ensuring a high isotopic purity ($> 95\,\%$).

In order to minimize systematic uncertainties, it is important to keep the activity and therefore the column density of tritium gas stable on the order of 10^{-3}. Any parameters influencing the column density, such as injection pressure, pumping speed or beam tube temperature need to be stable on the same level. The column density has been optimized to a value of $5{\cdot}10^{17}$ molecules/cm^2 by on the one hand maximizing the activity (10^{11} Bq) and on the other hand minimizing the energy loss due to scattering off molecules inside the source.

The β-electrons are guided towards the spectrometers on one side and the rear section on the other side by 3.6 T superconducting solenoid magnets. As the probability for inelastic scattering off T_2 molecules increases with higher starting angles relative to the magnetic field lines, the ratio of the magnetic field strengths of the WGTS magnets and the pinch magnet at the detector is chosen such that electrons with a starting angle of more than 51° are magnetically reflected.

At the control and monitoring section (CMS) at the rear end, the electrons are detected to monitor the activity of the tritium source.

2.2. Transport section

In order to achieve the required low background of 10 mcps at the main spectrometer[3], essentially all tritium molecules need to be pumped out. That is the main task for the transport section, along with the transport of the β-electrons from the source to the pre-spectrometer. In the first part, the differential pumping section (DPS) [47] reduces

[3]“cps“ stands for ”counts per second“, a commonly used unit for count rates

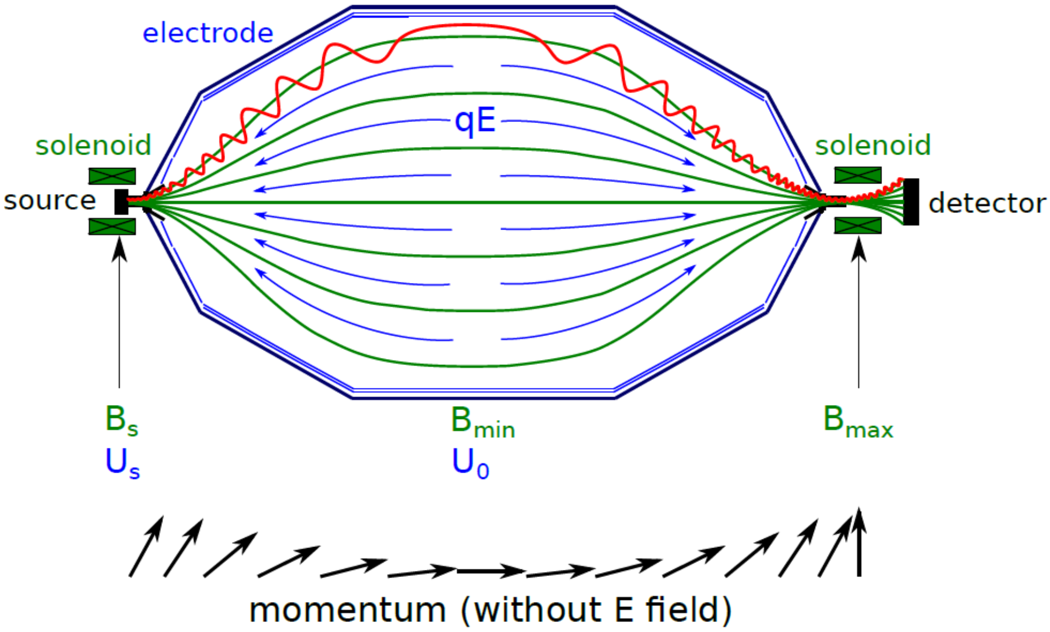

Figure 2.3.: Working principle of a MAC-E filter: Electrons (red) are guided from the source to the detector along the magnetic field lines in a cyclotron motion. As the magnetic field drops, their transverse energy gets transformed into longitudinal energy as illustrated via the momentum vector in the lower part. The electrostatic field acts as a high-pass filter. Figure from [49].

the tritium flow by a factor of 10^5. This is done actively by four turbomolecular pumps (TMP's). In the second part, the cryogenic pumping section (CPS) [48], remaining T_2 molecules are passively adsorbed at the inner surface of the CPS tube, which is kept at a temperature of 4.5 K and covered by a thin argon frost layer.

2.3. Spectrometers

The KATRIN setup contains two MAC-E filter spectrometers in the beam line and a separate third spectrometer for monitoring purposes. At first, the MAC-E filter principle will be explained in section 2.3.1 before the tasks of each spectrometer will be described in sections 2.3.2-2.3.4.

2.3.1. MAC-E Filter

Spectrometers of MAC-E filter type have been used and developed for measurements of the electron neutrino mass both in the Mainz and Troitsk experiment independently [42, 43]. Such a spectrometer basically works as a high-pass filter letting only electrons above a certain energy pass through. The working principle is illustrated in Figure 2.3. An axially symmetric inhomogeneous magnetic field is generated by two superconducting solenoids at both ends of the spectrometer. Electrons coming from the source, are guided along the magnetic field lines performing a cyclotron motion due to the Lorentz force. The magnetic field drops by several orders of magnitude from the source to the middle of the spectrometer called the analyzing plane, before it rises again towards the exit at the detector side, where it has its maximum $B_{\max}$. As the change of the magnetic field is relatively slow, the magnetic moment μ is constant (in the non-relativistic approximation):

$$\mu = \frac{E_\perp}{B} = const. \tag{2.1}$$

The transverse part of the energy of the electrons thereby transforms into longitudinal energy from the source to the analyzing plane and in the same way transforms back into transverse energy from the analyzing plane to the detector, as illustrated by its momentum vector in the lower part of Figure 2.3.

The energy selection is done by applying an electrostatic retarding potential U_0 to both the spectrometer vessel and an inner electrode system. Only electrons with sufficient longitudinal energy pass the potential barrier and are reaccelerated towards the detector, the rest is reflected back to the source. Due to the magnetic adiabatic collimation described above, the transformation of the transverse energy into longitudinal energy is maximal in the analyzing plane, where the electric field is parallel to the magnetic field lines. Therefore a MAC-E filter has a good angular acceptance and high energy resolution. The energy resolution is defined by:

$$\frac{\Delta E}{E} = \frac{B_{\min}}{B_{\max}}. \tag{2.2}$$

For the KATRIN main spectrometer that results in an energy resolution of $\Delta E = 0.93\,\mathrm{eV}$ for electrons close to the endpoint region.

2.3.2. Pre-spectrometer

The pre-spectrometer is 3.4 m long, has a diameter of 1.7 m and an energy resolution of $\Delta E \approx 70\,\mathrm{eV}$ at $E = 18.6\,\mathrm{keV}$ (see Figure 2.4). It can be operated on a potential of up to $-18.3\,\mathrm{kV}$ in order to reject electrons with lower energies, therefore acting as a pre-filter. The two superconducting solenoid magnets at both ends generate a magnetic field of 4.5 T. Until 2011, test measurements have been performed at the pre-spectrometer in order to investigate background mechanisms, electron transport and several other aspects [50–53].

2.3.3. Main spectrometer

The KATRIN main spectrometer is the largest component of the experiment. It is 24 m long and has a diameter of 10 m, resulting in a total volume of about 1250 m^3. In here, the precision measurement of the endpoint region of the tritium β spectrum takes place. The two solenoid magnets at the pre-spectrometer together with the pinch magnet and the detector magnet, both at the detector side of the spectrometer, generate the magnetic field along which the electrons are guided to the detector. There is an additional system of air coils (LFCS[4]) surrounding the spectrometer vessel. A different voltage can be assigned to

[4]**L**ow **F**ield **C**orrection **S**ystem

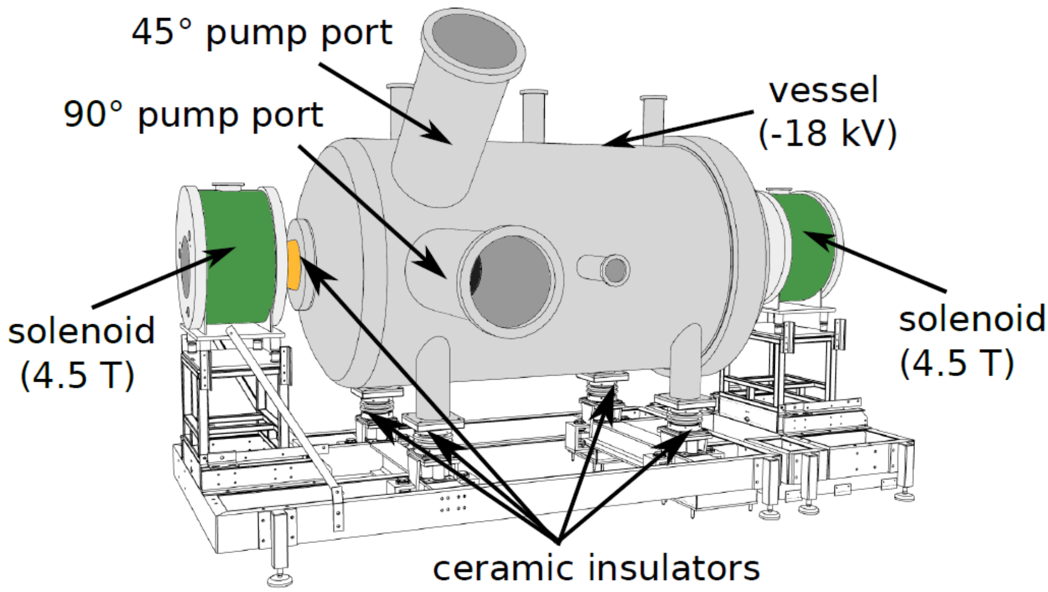

Figure 2.4.: The pre-spectrometer serves as a pre-filter for the low-energy electrons. A magnetic guiding field is provided by the two superconducting solenoid magnets at both sides. Figure from [51].

each air coil individually in order to fine tune the magnetic field. Furthermore, the Earth's magnetic field is compensated by the EMCS[5] [54].

Both the pre-spectrometer and the main spectrometer are operated under ultra high vacuum conditions (10^{-11} mbar) in order to minimize both the background due to ionization of residual gas molecules and the energy loss of β-electrons due to scattering off residual gas molecules. For that purpose, six TMPs for active pumping and over 3000 m of non-evaporable getter (NEG) strips passively pumping mainly H_2 molecules [55, 56] have been installed. As the pre-spectrometer, the main spectrometer vessel itself can be set to high voltage. On the inside of the main spectrometer is an almost massless inner wire electrode system [53, 57] installed in order to fine tune the voltage generating the electrostatic field and to reduce the background induced by charged particles coming from the 650 m^2 large surface.

2.3.4. Monitor spectrometer

The monitor spectrometer, which is essentially the former Mainz spectrometer, is set up in a separate building next to the main spectrometer. It is fed by the same high voltage as the main spectrometer therefore providing a monitoring device for the high voltage stability [58, 59]. A krypton source (^{83m}Kr/K32 line) is used to measure the stability of the high voltage.

[5]**E**arth **M**agnetic field **C**ompensation **S**ystem

2.4. Detector system

The electrons that manage to reach the downstream end are counted by the focal plane detector (FPD) [60]. It is a silicon PIN-diode segmented into 148 pixel with a sensitive diameter of 9 cm and a thickness of about 500 μm. The FPD provides a spatial, timing and energy resolution. It is very important to achieve an extremely low intrinsic detector background in order to reach the required sensitivity. Therefore the FPD is operated under ultra high vacuum conditions, the hardware components of the detector system are chosen such that they have a low intrinsic radioactivity and the detector is surrounded by a passive shield made of lead and copper to protect it from environmental radiation. Additionally an active veto system consisting of plastic scintillators enables the rejection of cosmic ray background via muon tagging. There is a post-acceleration electrode which can shift the energy of the electrons up to 30 keV towards higher energies in order to obtain a better signal to background ratio. An ^{241}Am source and a UV-illuminated titanium disc are used for calibration. For further information on the detector system see [46, 61].

2.5. Background sources

A very good understanding of the background sources at the KATRIN spectrometers and their reduction is essential in order to achieve the aspired neutrino mass sensitivity of 200 meV/c^2. Therefore several commissioning measurements have been done and will be done in the near future with the goal to investigate the background and reach the required background level of the order of 10 mcps. The two main background sources expected from previous measurements with spectrometers of MAC-E filter type will be described in this section.

2.5.1. Magnetically stored particles

The main disadvantage of a MAC-E filter is, that there is a rather high probability for charged particles, being produced inside the spectrometer, to get stored due to the magnetic mirror effect. Storage times are on the order of minutes to hours, depending on the initial energy of the stored particle and the pressure inside the spectrometer. During that time it can produce further electrons via ionization of residual gas molecules. These low energetic electrons are usually not stored and reach the detector with an energy in the same region as the signal electrons.

The dominant source for such electrons being produced in the spectrometer volume are the radon isotopes ^{219}Rn and ^{220}Rn [46, 49, 51, 62]. They mainly originate from the NEG pumps and decay inside the volume due to their short half-lives ($\tau_{1/2}^{219} \approx 4$ s, $\tau_{1/2}^{220} \approx 56$ s) emitting electrons before they can be pumped out. As a passive countermeasure against the radon induced background, liquid nitrogen cooled baffles have been installed in the pump ports between the spectrometer volume and the NEG pumps [63, 64].

Although the tritium flow gets reduced by 14 orders of magnitude, a small fraction can still reach the spectrometer and thus produce high energetic electrons that can also get stored and therefore increase the background[65].

2.5.2. Secondary electrons from the surface

Secondary electrons coming from the spectrometer wall and the inner wire electrodes are expected to be another major background source. These secondaries are expected to be primarily induced by cosmic muons, but also high energy photons from environmental radioactivity can interact with the inner surfaces producing low energetic secondary electrons [49, 66].

There is also the possibility of field emission. Irregularities in the surface and sharp edges at the inner wire electrodes can lead to high electric field strengths within a very narrow region enabling electrons to leave the surface via the tunnel effect. There are two shielding mechanisms against secondary electrons. One is magnetic shielding due to the axially symmetric magnetic flux tube (see section 5.1) and the other one electrostatic shielding due to the inner wire electrodes (see section 5.2).

However, small inhomogeneities in electric and magnetic fields can not be avoided and therefore some of the secondaries can drift inside the flux tube and reach the detector with energies in the same region as the β-electrons. An explanation of this drift process can be found in [66]. Within this thesis the muon induced part of the secondaries and their influence on the background has been investigated.

3. The muon detector system at the main spectrometer

Secondary electrons from cosmic ray muons are expected to be one of the major background sources at KATRIN, as the experiment has been built above ground and the main spectrometer has a rather large surface of approximately $650\,\mathrm{m}^2$. In order to be able to investigate the muon induced background component, a detector system to measure the muon flux has been installed next to the main spectrometer [67]. The muon detector modules were originally used at the KARMEN [68] experiment and have been modified for the use at KATRIN. There are eight large modules with dimensions of $3.15\,\mathrm{m} \times 0.65\,\mathrm{m} \times 0.05\,\mathrm{m}$ corresponding to a sensitive area of $2.05\,\mathrm{m}^2$ each and one small module with a sensitive area of $0.3\,\mathrm{m}^2$. In Figure 3.1 one of the large modules can be seen. Muons passing through the scintillator produce photons which leads to a signal at the photomultiplier tubes (PMTs[1]) at both ends. The locations of the modules are shown in Figure 3.2. They were positioned such that mainly muons passing through the main spectrometer are detected in order to be able to look for direct coincidences between muons crossing the spectrometer and background electrons reaching the detector. In the following sections the muon detector system, its main features and some characteristics will be described in more detail.

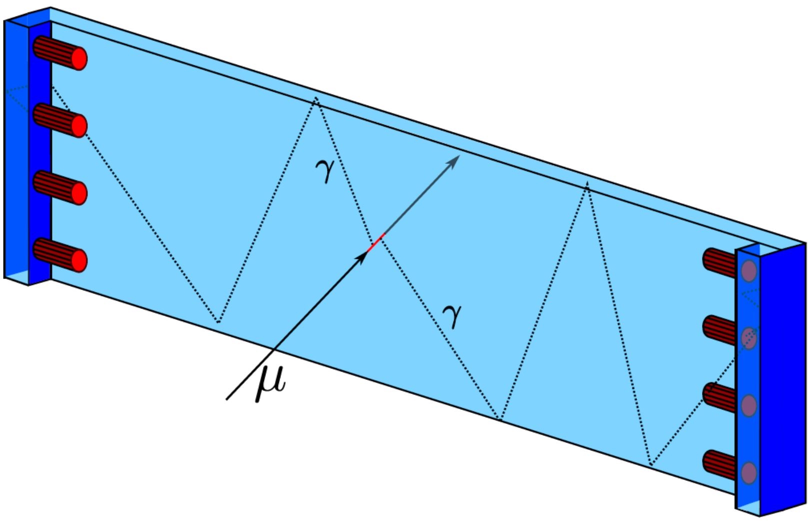

Figure 3.1.: Schematic drawing of a muon module with four photomultiplier tubes at both ends [49].

[1]Type: 2" Philips VALVO XP 2262

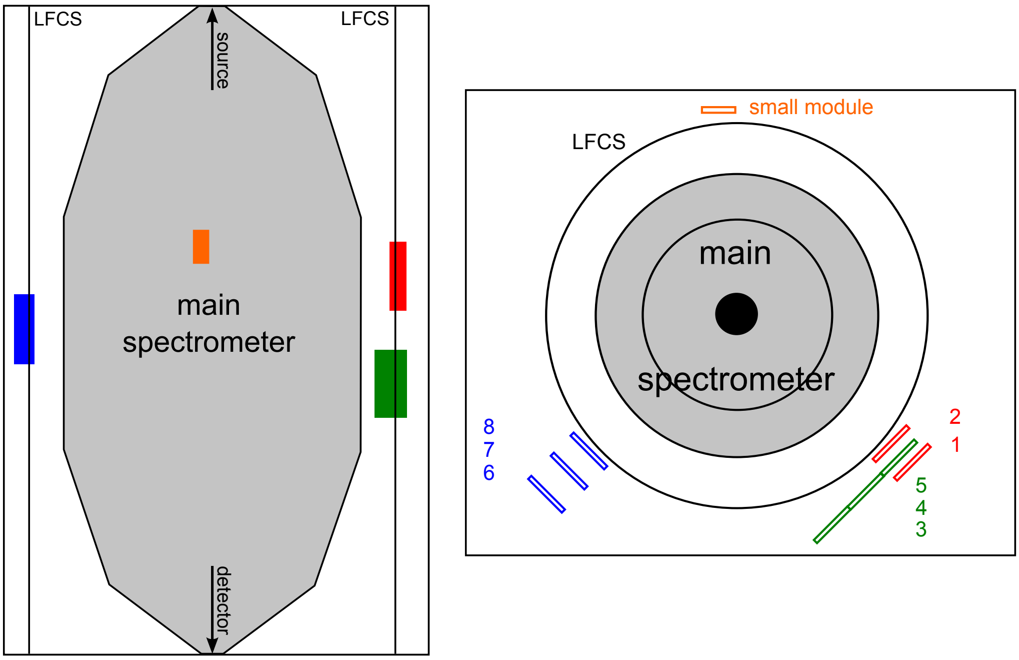

Figure 3.2.: Positions of the muon detector modules relative to the main spectrometer. Based on [69].

3.1. Scintillator

The modules consist of the organic plastic scintillator BICRON BC-412, which has a very good absolute photon yield of about 8.5 photons/keV [68]. When a high energy photon or a charged particle like in this case a muon passes through scintillating material, photons are emitted. In order to minimize the photon loss due to the transportation inside the modules, they are wrapped in wrinkled aluminum foil. Additionally they are surrounded by black polyethylene foil which is impermeable to light. At both ends of the eight large modules four photomultiplier tubes (PMT) are installed, the small module has two PMTs at one end.

3.2. Photomultiplier

Photomultipliers are commonly used to detect very low light fluxes as they are able to produce a signal even out of a single photon via photoelectric effect and secondary emission of electrons in a vacuum tube. The working principle of a PMT is illustrated in Figure 3.3. When a photon hits the photocathode, an electron is emitted due to the photoelectric effect. The photoelectron then hits a series of dynodes, producing additional electrons at each dynode via secondary emission. As the modules are situated in the vicinity of the air coils and hence are exposed to high magnetic fields of up to 1 mT, the PMTs are magnetically shielded with several layers of permalloy foil. The PMTs are operated on high voltage of about 1.5 kV, a detailed list of the used voltages can be found in Appendix A.

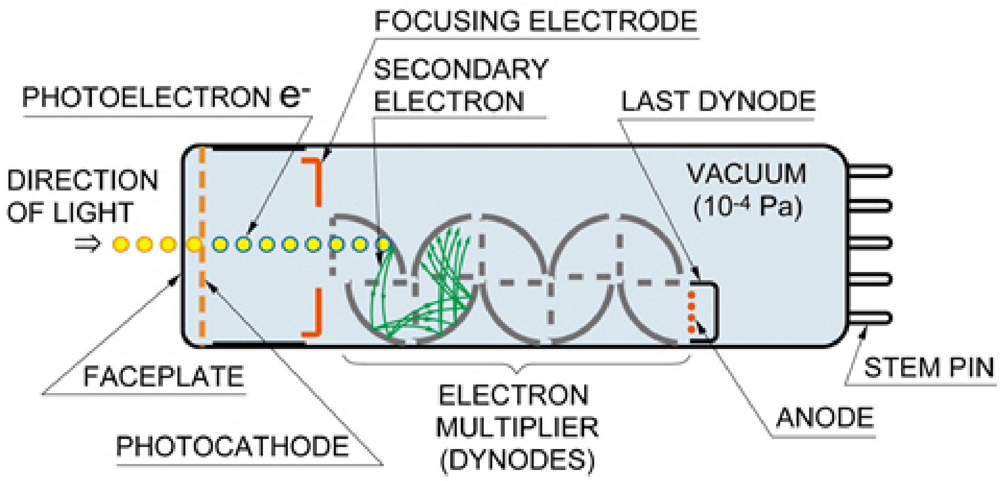

Figure 3.3.: Working principle of a PMT [70].

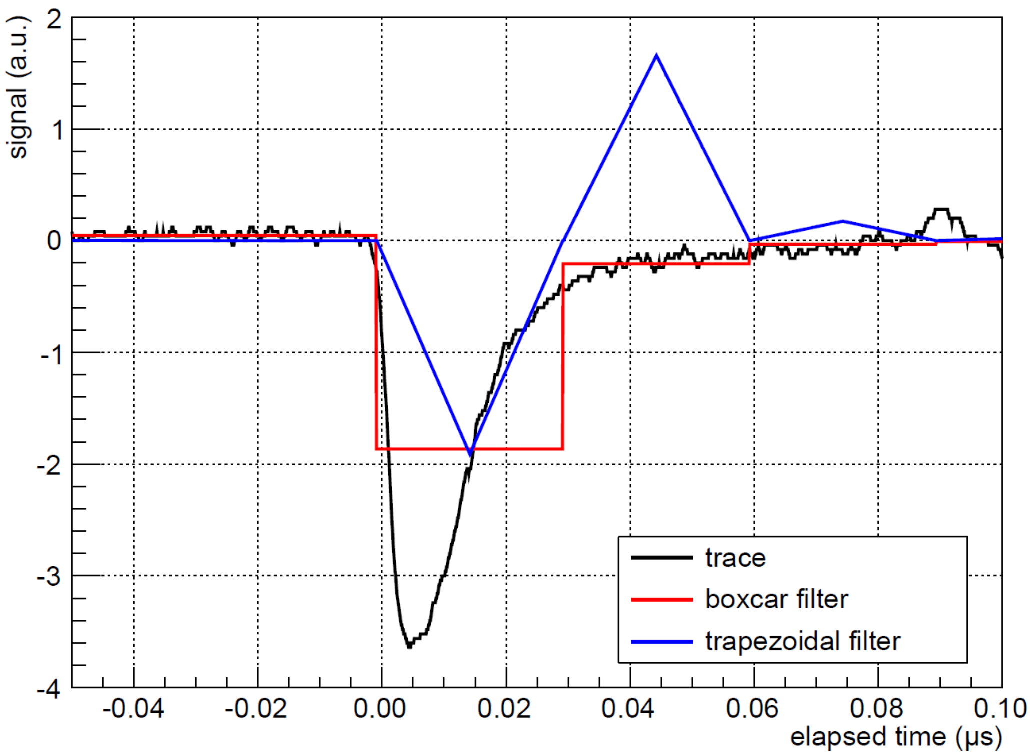

Figure 3.4.: Example signal with both first and second stage filter output. The time interval is set to $t_{BC} = 30\,\text{ns}$. Figure adapted from [69].

3.3. DAQ System

At each side of a module the signals of all four PMTs are added and guided to the data acquisition (DAQ) crate[2] by a coaxial cable. The first level trigger (FLT) card only passes events that are recorded at both ends of a module on to the second level trigger (SLT). The Object-oriented Real-time Control and Acquisition (ORCA) [71] software then stores the event data in a file. A list of the DAQ channel assignments can be found in Appendix A. In order to be able to investigate direct coincidences between cosmic muons hitting the spectrometer surface and secondary electrons reaching the FPD, an accurate timing is essential. Therefore the muon detector DAQ and the focal plane detector DAQ are synchronized by a high precision clock. A precise determination of the muon event time is achieved by applying a boxcar filter followed by a trapezoidal filter to the signal of the photomultipliers (see Figure 3.4). The boxcar filter first takes the floating average $BC(t)$ of the signal over a preset time interval t_{BC}. If $BC(t)$ exceeds a certain trigger level, the filtered signal is run through the second filter. This trapezoidal filter with shaping length t_{T} subtracts the integrals of the first half of the time window and the second half from each other. The event time is then determined via the zero crossing of the trapezoidal filter signal [66].

3.4. Calibration of the muon modules

The muon modules have been calibrated with the main purpose being to set the trigger thresholds to approximately the same energy for both sides of all muon modules. In order to do so, a ^{60}Co source has been attached to different positions on the modules as can be seen in Figure 3.5. ^{60}Co decays mainly into an excited state of ^{60}Ni, which then subsequently emits two gamma rays while falling into the ground state. The energy of these two gammas accounts to 1.17 MeV and 1.33 MeV respectively. As the muon modules can not resolve such a small difference in energy, the average of 1.25 MeV has been taken for the calculations.

In Figure 3.6a the event counts are plotted over the ADC value, which is proportional to the energy, for all three source positions of the ^{60}Co source at side A of module 6.

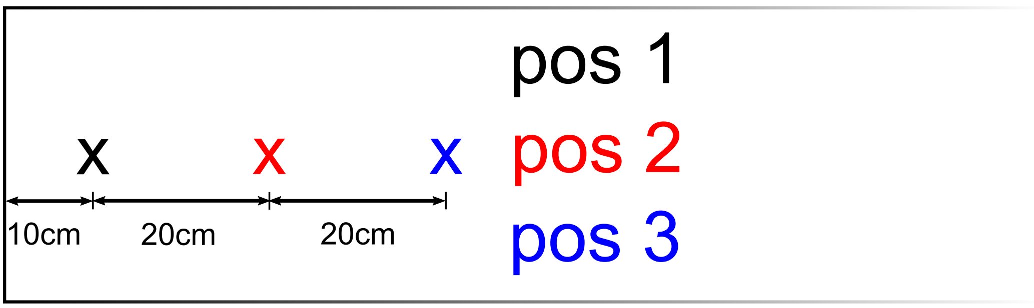

Figure 3.5.: Sketch of the ^{60}Co source positions for calibration measurements.

[2] IPE-4, designed and constructed at IPE, KIT

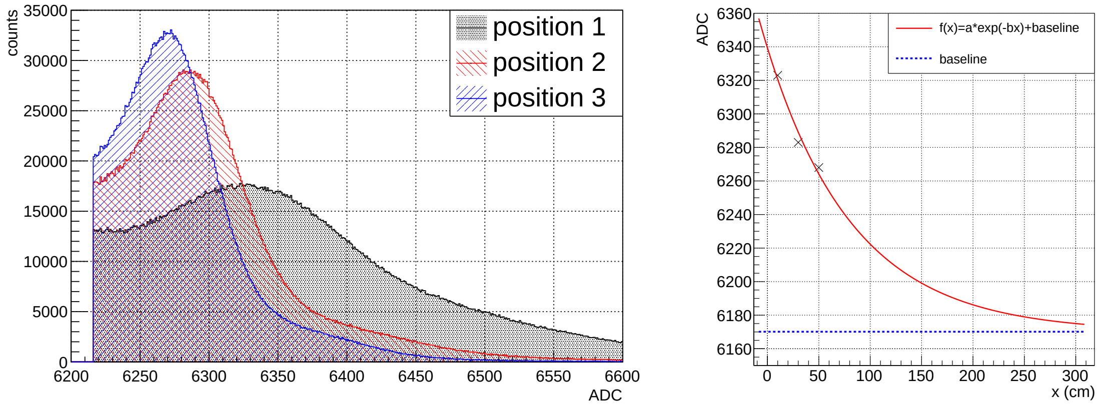

(a) **(b)**

Figure 3.6.: a) ADC histogram for all 3 source positions at module 6A. **b)** ADC peak values over source positions for the same module. An exponential fit has been applied and the baseline is shown as well.

The exponential background present at lower energies has already been subtracted. As expected the peak position shifts from higher energies to lower energies the farther away the source gets from the end of a module and therefore from the PMTs. The peak width accounts for the different path lengths from the source to all four PMTs. Thus, the closer the source gets to the PMTs the bigger the differences of the path lengths, hence a broader energy distribution. The peak positions, which have been determined by fitting a Gaussian to the corresponding ADC spectra, have been plotted over the distance of the source from the end of the module (Figure 3.6b). To estimate the ADC value corresponding to the energy of the gamma radiation from the ^{60}Co source, the following exponential function has been fitted:

$$f(x) = a \cdot e^{-bx} + \text{baseline}, \tag{3.1}$$

where a and b are free parameters and the baseline has been determined for each channel in a different measurement. The extrapolated ADC value at zero distance has been taken as equivalent to the average energy of the two gammas. With the assumption of a linear behavior the ADC values could now be transformed into energy values. Figure 3.7 shows the resulting energy spectrum for a 1 h run split into individual channels. It should be kept in mind, however, that this method just gives a rough estimate, as small distance variations near the PMTs result in a large energy variation due to the exponential shape of the fit function. Also the assumption of a linear behavior might not be accurate.

3.5. Efficiency of the muon modules

The efficiency of the muon modules was determined with a dedicated measurement configuration. However, for technical reasons this could only be done for the modules 1 to 5. Five measurements have been performed with three modules set up right on top of each other (see Figure 3.8) so that each one was situated in the middle for one run. That

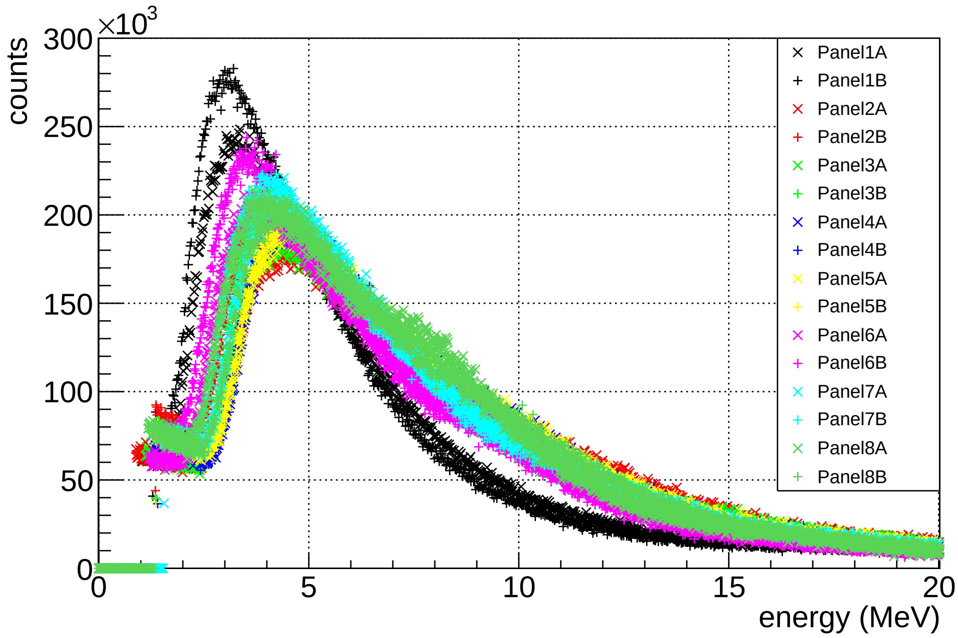

Figure 3.7.: Energy spectrum of all muon modules, split into individual channels.

way the efficiency of those five modules could be determined according to the formula derived in the following paragraph.

The efficiency is defined by

$$\epsilon = \frac{R^{\text{measured}}}{R^{\text{real}}},$$

where R^{measured} and R^{real} are the measured and real rate respectively and ϵ is the efficiency. Thus for three coaligned modules A, B and C with B being the middle one, it follows that

$$R^{\text{measured}}_{\text{ABC}} = \epsilon_{\text{A}} \cdot \epsilon_{\text{B}} \cdot \epsilon_{\text{C}} \cdot R^{\text{real}} \tag{3.2}$$

$$R^{\text{measured}}_{\text{AC}} = \epsilon_{\text{A}} \cdot \epsilon_{\text{C}} \cdot R^{\text{real}}, \tag{3.3}$$

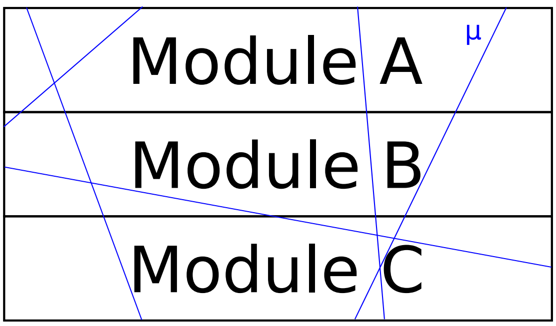

Figure 3.8.: Sketch of the muon module arrangement used for the efficiency measurements.

where $R_{\mathrm{ABC}}^{\mathrm{measured}}$ is the measured coincidence rate of muons detected by all three modules and $R_{\mathrm{AC}}^{\mathrm{measured}}$ is the measured coincidence rate of muons detected only by the upper and lower module. As the modules are placed right on top of each other (see Figure 3.8, all muons crossing modules A and C must have passed through module B as well. Dividing (3.2) by (3.3) the efficiency of module B is obtained:

$$\epsilon_{\mathrm{B}} = \frac{R_{\mathrm{ABC}}^{\mathrm{measured}}}{R_{\mathrm{AC}}^{\mathrm{measured}}}. \tag{3.4}$$

For module 7 the same calculation has been done, as modules 6 to 8 are installed on top of each other. There is some space between them and they are inclined by a 45° zenith angle, but the assumption that muons passing through module 6 and 8 must have gone through module 7 as well should still hold. As the results listed in Table 3.1 show, the efficiency is very high for all measured modules.

Table 3.1.: Results of efficiency measurements.

Module	Efficiency (%)
1	99.2 ± 0.3
2	99.2 ± 0.3
3	99.2 ± 0.3
4	99.2 ± 0.3
5	99.2 ± 0.3
7	95.1 ± 0.4

4. Cosmic muon flux variations

The cosmic muon flux at sea level is known to fluctuate in time depending on various factors [75]. Some of these factors can be associated with fluctuations of the primary cosmic ray flux, but atmospheric conditions also need to be considered for the muon flux variations. Therefore, an introduction into cosmic rays will be given in section 4.1 and the main influences on the muon flux at sea level will be discussed in section 4.2. Measurements of these variations with the KATRIN muon detection system will then be presented in section 4.3.

4.1. Cosmic rays

The existence of cosmic rays has first been discovered by the Austrian physicist V. Hess during his balloon measurements at altitudes of up to 5 km in 1911/1912 [76]. About 85 % of the charged primary cosmic rays are protons, about 12 % are α-particles, the rest are heavier nuclei and electrons. The energy spectrum of cosmic rays above an energy of 10^{14} eV is shown in Figure 4.1. At such high energies, primary cosmic rays can not be measured directly any more. When those primary cosmic particles interact with molecules of the upper atmosphere, a cascade of secondary particles, a so called Extensive Air Shower (EAS), is produced (see Figure 4.2). Ground based experiments like KASCADE[1] [77] or the Pierre Auger Observatory [78] have been built to measure those secondary particles.

At an altitude of 15 to 20 km, depending on the particle species and its energy, the first interactions take place leading to electromagnetic or hadronic cascades [79]. In case of a proton, a hadronic cascade is initiated in the 100 mbar layer, which corresponds to a height of approximately 16 km in the International Standard Atmosphere (ISA)[2]. The primary proton produces mainly pions and kaons (10 % compared to pions) [79]. Depending on their energy, they can either interact with the air molecules or decay as follows:

$$\begin{aligned} \pi^0 &\rightarrow \gamma + \gamma \\ \pi^\pm / K^\pm &\rightarrow \mu^\pm + \overset{(-)}{\nu}_\mu \end{aligned} \tag{4.1}$$

The neutral pions contribute to the electromagnetic component of the shower, whereas the charged pions are responsible for the muons and neutrinos. As the electromagnetic component is absorbed in the atmosphere relatively quickly, the composition of cosmic ray particles at sea level is dominated by muons and neutrinos (see Figure 4.3).

[1]**KA**rlsruhe **S**hower **C**ore and **A**rray **DE**tector

[2]The ISA is a model for the change of pressure, temperature, density and viscosity with altitude in the Earth's atmosphere. The actual height of the 100 mbar layer at a specific place to a certain time can deviate significantly from that value.

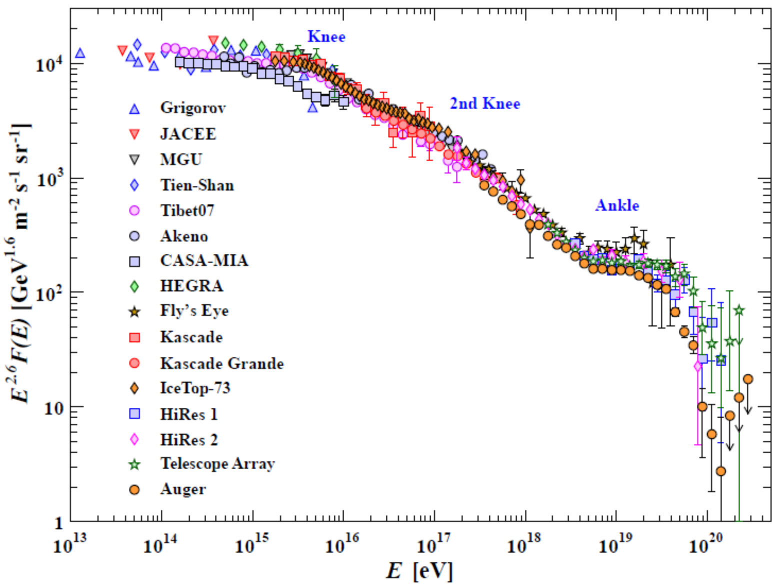

Figure 4.1.: Energy spectrum of cosmic rays above 10^{14} eV scaled by a factor of $E^{2.5}$ for a better visibility of the knee around 10^{15} eV and the ankle around 10^{19} eV. A second kneelike feature around 10^{17} eV has been found not long ago by the KASCADE-Grande collaboration [72]. Figure from [73].

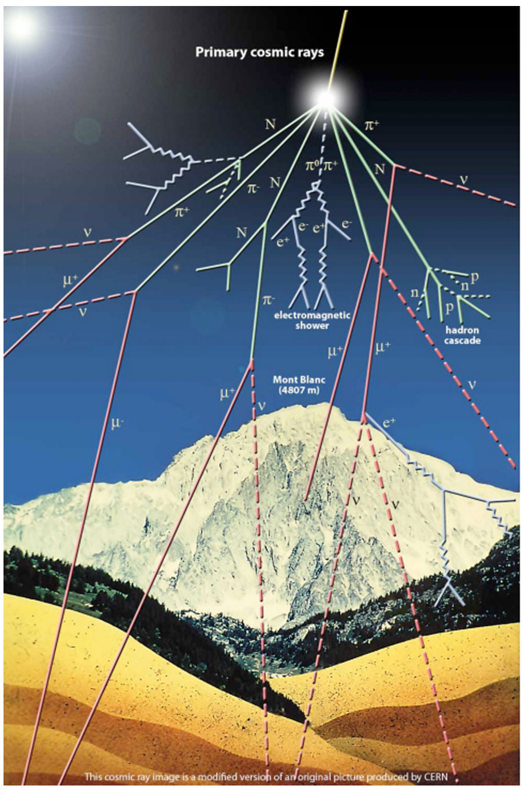

Figure 4.2.: Schematic picture of an Air Shower. Figure taken from [74].

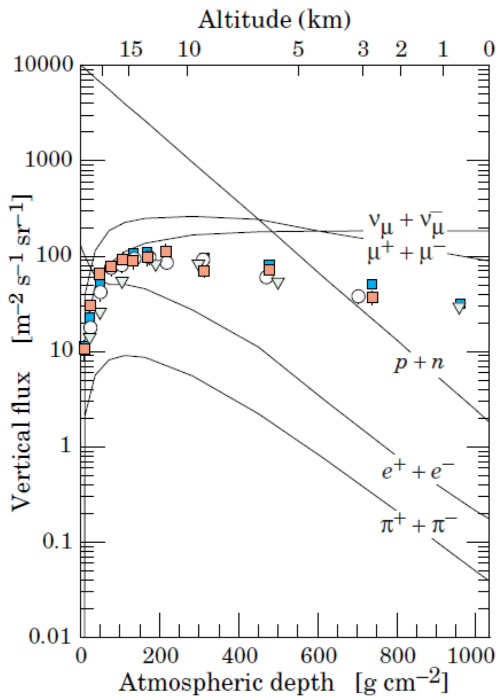

Figure 4.3.: Composition of vertical cosmic rays at sea level with an energy > 1 GeV. The points are from measurements of negative muons. Figure from [73].

Muons are mainly produced at a production height of 15 km and typically lose about 2 GeV via ionization on their way to sea level, where they have a mean energy of about 4 GeV [73]. The fact that they are able to survive over such a long distance despite their lifetime of only 2.2 µs is due to the relativistic time dilation:

$$\tau = \gamma \tau_0 = \frac{E}{m_0} \tau_0, \tag{4.2}$$

where γ is the Lorentz factor, E the total muon energy and m_0 its rest mass. In case of a 4 GeV-muon that results in a lifetime of $\tau = 83.3$ µs. For further information about cosmic rays see [80].

4.2. Variations of the muon flux at sea level

There are basically three different influences leading to variations of the cosmic muon flux at sea level:

- Solar modulation of the primary cosmic rays
- Atmospheric conditions
- Geomagnetic latitude

The last point will not be considered here, as it accounts for changes in the muon flux when changing the location of the detector, which is not the case here.

When galactic cosmic rays enter the heliosphere, they are strongly influenced by solar magnetic fields and the solar wind. The influence is stronger for particles with lower energies and weaker for high energetic particles. Solar modulations can be split into two categories, periodic and sporadic. The solar activity of the Sun has an 11-year cycle leading to periodic variations of up to 30 % on large time scales. Another periodic variation arises from the rotation of the Sun with a period of 27 days and variations of less than 2 %. A diurnal variation of a few % can also be observed which is due to a spatially anisotropic particle stream. With the rotation of the Earth, the field of view of the muon detector passes that anisotropy once a day. The most important aperiodic effects are the Forbush decrease resulting from solar magnetic disturbances with an amplitude of up to 30 % and solar eruptions, where solar particles cause the flux to increase up to 300 % [81, 82].

The muon flux variations due to atmospheric conditions can be described by changes in the atmospheric pressure in the 100 mbar layer Δp, the altitude of the main muon production layer ΔH and the temperature in the region between the 100 and 200 mbar layers ΔT in the following way:

$$\frac{\Delta I}{I} = -\left(\alpha_\mu \cdot \Delta p + \beta \cdot \Delta H - \gamma \cdot \Delta T\right). \tag{4.3}$$

Here, $\alpha_\mu = 0.16$ %/mbar is the barometric pressure coefficient, $\beta = 5$ %/km is the decay coefficient and $\gamma = 0.1$ %/K is the atmospheric temperature coefficient [83].

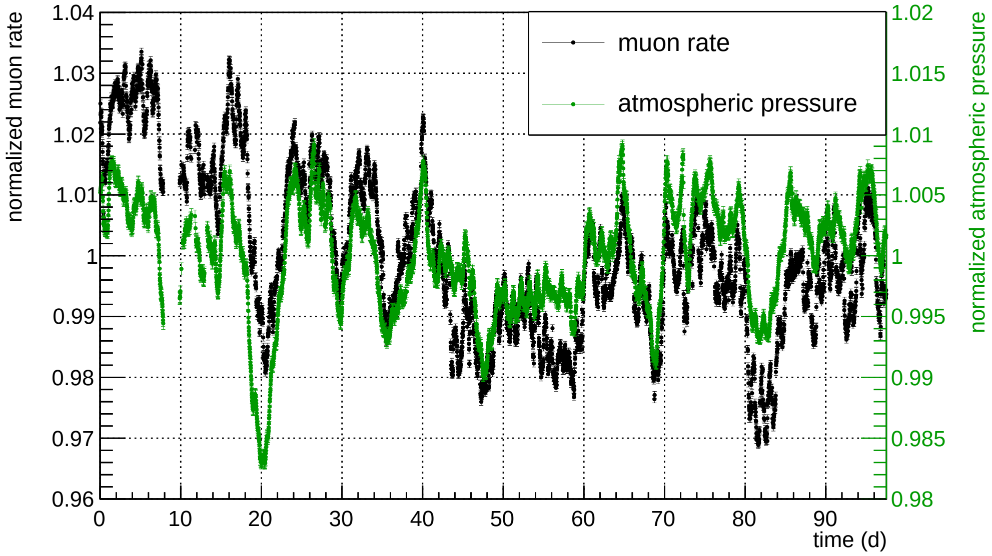

Figure 4.4.: Normalized muon rate (black, left axis) over time in a period of 3 months from the end of April until the end of July 2014. Fluctuations of up to ±3.5 % can be seen. The atmospheric pressure at KIT Campus North, multiplied by −1 and normalized is plotted as well (green, right axis). Their anticorrelation corresponds to $r = -0.64$.

4.3. Measurements of muon rate variations at KATRIN

From the 25th of April until the 1st of August 2014, a longterm measurement has been performed with the KATRIN muon detector system (see also [66, 69]). In Figure 4.4, the muon rate together with the atmospheric pressure[3] have been plotted. The atmospheric pressure was multiplied by −1, as an anticorrelation is expected. Both data sets were normalized to their mean value, which correspond to (1590.0±0.3) cps for the muon rate and 1002.07 mbar for the atmospheric pressure. Module 2 has been excluded in this analysis due to performance issues. Fluctuations of up to ±3.5 % can be seen in the muon rate and up to ±2 % in the atmospheric pressure. A rather high anticorrelation is already visible, therefore the sample Pearson correlation coefficient has been calculated via

$$r = \frac{\sum_{i=1}^{n} (x_i - \bar{x})\,(y_i - \bar{y})}{\sqrt{\sum_{i=1}^{n} (x_i - \bar{x})^2}\,\sqrt{\sum_{i=1}^{n} (y_i - \bar{y})^2}} \tag{4.4}$$

where $x_1, \ldots x_n$ and $y_1, \ldots y_n$ are two datasets and $\bar{x}$ and $\bar{y}$ are the corresponding mean values. For the correlation between the muon rate and the pressure this results in a value of $r = -0.64$. A clear correlation to temperature data measured at an altitude of 2 m above ground could not be found, which is expected, as the muon flux is influenced by the atmospheric conditions at an altitude of about 15 km, where the temperature fluctuations are different.

[3]Data of pressure and temperature was kindly provided by the Institute of Meteorology and Climate Research - Troposphere Research from the 200 m meteorological tower at KIT Campus North.

The diurnal variation can also be seen by taking a look at smaller time scales of 7 days. This is shown in Figure 4.5, where a zoom into an arbitrarily chosen time frame of a week is displayed. The peaks are approximately around 2 p.m. local time (CEST).

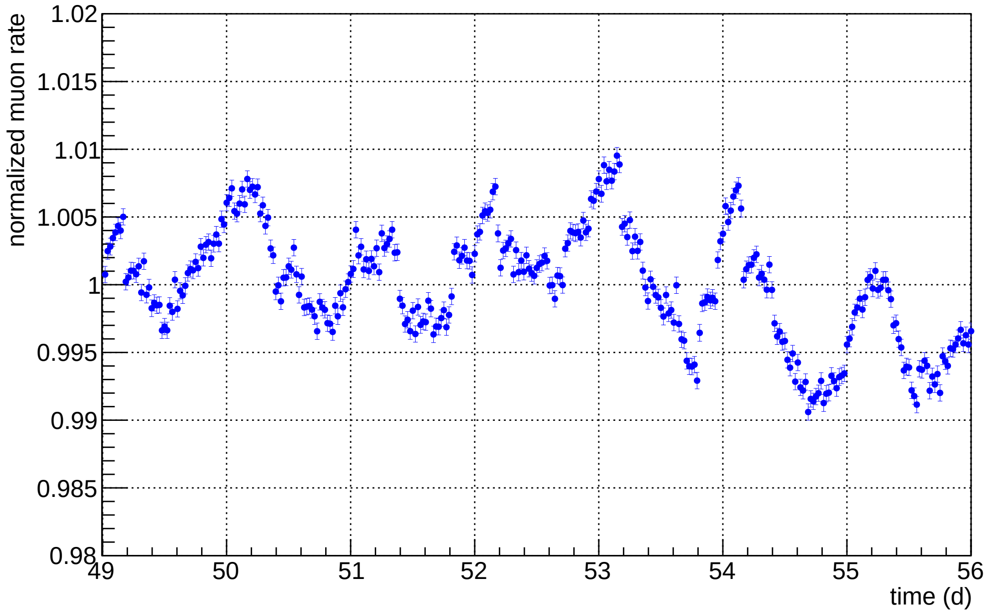

Figure 4.5.: Zoom into the normalized muon rate in a time frame of a week. The diurnal variations can clearly be seen.

5. Background measurements at the main spectrometer

An important measurement of the second SDS[1] commissioning phase was a longterm background measurement with parallel operation of main spectrometer and muon detector system. The goal of this measurement was to investigate the correlation between cosmic muons running through the spectrometer and background electrons reaching the detector. In order to minimize spectrometer backgrounds due to charged particles from the spectrometer walls, the KATRIN main spectrometer utilizes magnetic shielding (section 5.1) and electrostatic shielding (section 5.2) mechanisms. The settings used for the SDS-II longterm measurement are described in section 5.3. Results of standard background analyses for this measurement are presented in section 5.4. The correlation to the muon rate will be investigated in chapter 6.

5.1. Magnetic shielding

A very effective suppression of muon induced background is already provided by the MAC-E filter itself, as charged particles in magnetic fields are deflected by the Lorentz force. The shielding factor due to the axially symmetric magnetic field (see Figure 5.1) is expected to be of the order of 10^5 [49]. There are two types of secondary electrons coming from the wall of the spectrometer, high energetic fast secondaries and so called true secondaries with low kinetic energy.

Fast secondaries can pass through a rather large part of the flux tube before they are reflected back to the wall by the Lorentz force. However, they only contribute to the background via ionization of residual gas molecules which is negligible due to a small cross section and low pressure inside the spectrometer.

Low energetic true secondaries are reflected back to the wall almost immediately as long as the magnetic field lines run parallel to the vessel. There are three scenarios though for low energetic electrons with a small enough starting angle relative to the surface to perform rather long trajectories inside the spectrometer volume:

1. They can be guided along magnetic field lines outside the flux tube, not reaching the sensitive area of the detector.

2. Electrons starting near the analyzing plane can be stored, as they are reflected at both ends of the spectrometer due to the magnetic mirror effect.

[1] **S**pectrometer and **D**etector **S**ection

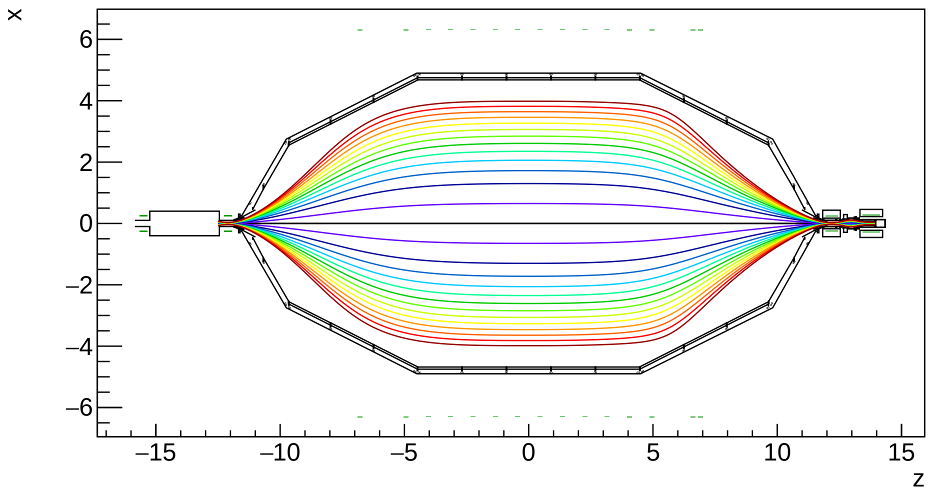

Figure 5.1.: Magnetic field lines in the 3.8 G symmetric setting. The spaces between two adjacent lines each correspond to a ring at the FPD.

3. In passing domains of low magnetic and high electric field, electrons can gain enough energy within a few cyclotron periods to perform non-adiabatic motions allowing them to drift inside the magnetic flux tube and reach the detector.

A more detailed description of the magnetic shielding and the processes allowing background electrons to still reach the detector can be found in [49, 66].

5.2. Electrostatic shielding

In order to further reduce the background due to charged particles from the wall, the main spectrometer is equipped with an inner wire electrode system for electrostatic shielding. A sketch of the double layer inner wire electrode (IE) system can be seen in Figure 5.2. Each layer can be set to an individual negative offset voltages relative to the tank potential. Electrons with energies less than 100 eV for example are not able to overcome an offset

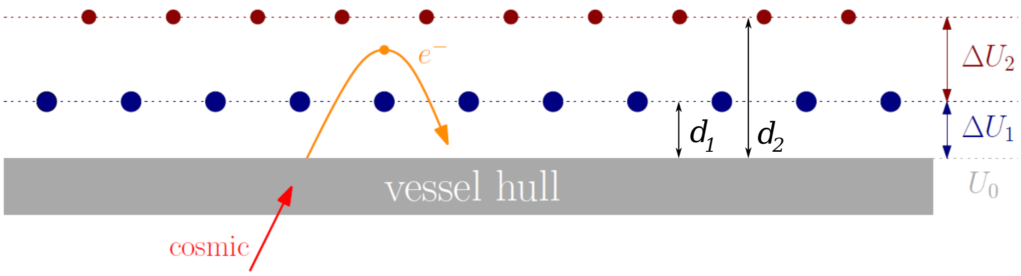

Figure 5.2.: Working principle of the double layer inner wire electrode. The distances of the electrodes to the wall are $d_1 = 15$ cm and $d_2 = 22$ cm respectively. Figure adapted from [66].

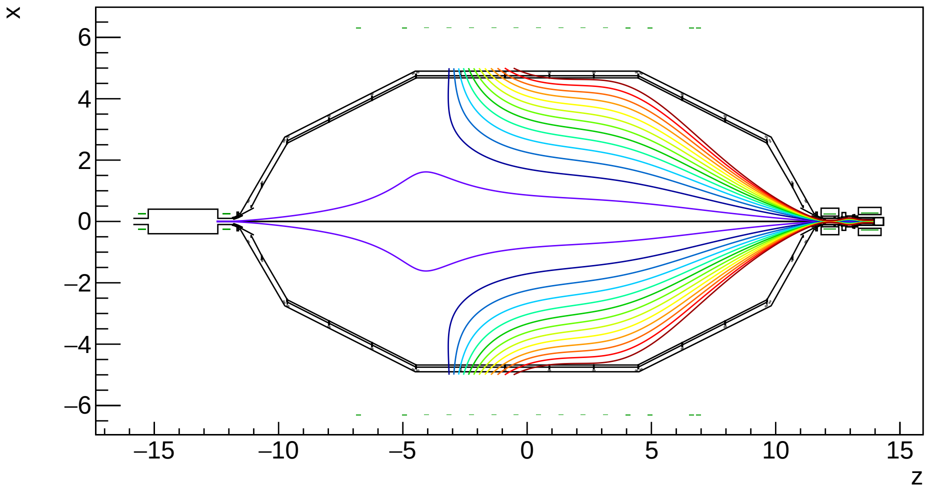

Figure 5.3.: Magnetic field lines in the asymmetric setting. Electrons from the wall are directly guided to the detector.

potential of 100 V and are therefore reflected to the wall. By setting the second layer to a more negative offset potential, the shielding is even more efficient. That way, electrons emitted from the support structure, which is the most massive part of the electrode system, are shielded as well. The electrostatic shielding is expected to reduce the muon induced background by another factor of 10^2 [49].

5.3. Measurement settings

Three different measurement settings have been chosen, in order to optimize the investigation of the muon induced background within a time period of two weeks. An automatic cyclic repetition of the three settings was achieved by executing an ORCA run script (see Appendix C). The advantage of cycling through the different settings as opposed to measuring each setting for several days in a row is that this way the muon flux variations of the whole two weeks are present in each different measurement configuration. An overview of the different settings is given in Table 5.1.

The steep cones are provided with an additional positive offset potential - with respect to the IE - to ensure that the transmission requirements are fulfilled and the spectrometer

Table 5.1.: Overview of the three different settings for the SDS-II longterm measurement.

Setting	Magnetic field configuration	Tank potential (kV)	IE offset (V)	steep cones offset (V)	Run time (s)
1	asymmetric	−18.6	−5	+2	1500
2	3.8 G symmetric	−18.6	−5	+2	5000
3	3.8 G symmetric	−18.5	−100	+97	5000

functions as a MAC-E filter with an energy resolution $< 1\,\text{eV}$. In all configurations, the post acceleration electrode was set to $4\,\text{kV}$. During the whole time, the radon induced background was efficiently reduced by two cold baffles [64, 84].

In measurement setting 1, the magnetic field lines directly connect the spectrometer vessel with the detector, thus guiding secondary electrons from the wall directly to the FPD (see Figure 5.3). A detailed list of the LFCS currents for the asymmetric field setup can be found in Appendix B. As it was not possible to completely turn the IE voltage off via the run script, it was set to the smallest stable value of $-5\,\text{V}$. The purpose of this setting was to maximize the rate of muon induced secondaries reaching the detector by removing magnetic and electrostatic shielding. The two settings with symmetric magnetic field served to investigate the remaining muon induced background with active magnetic shielding. Setting 2 was with reduced electrostatic shielding ($-5\,\text{V}$ inner electrode offset) and setting 3 with an electrostatic shielding of $-100\,\text{V}$.

As outlined in section 4.2, the fluctuations of the muon flux have a diurnal period. Thus, systematic effects may arise if the starting time of a whole cycle is in phase with the muon rate fluctuations. Therefore the run times have been chosen such that the starting times of the run cycles were equally distributed over the time of the day as can be seen in Figure 5.4. Only a few of the runs had to be excluded mainly due to sporadic loss of SlowControl set point values (see Appendix D).

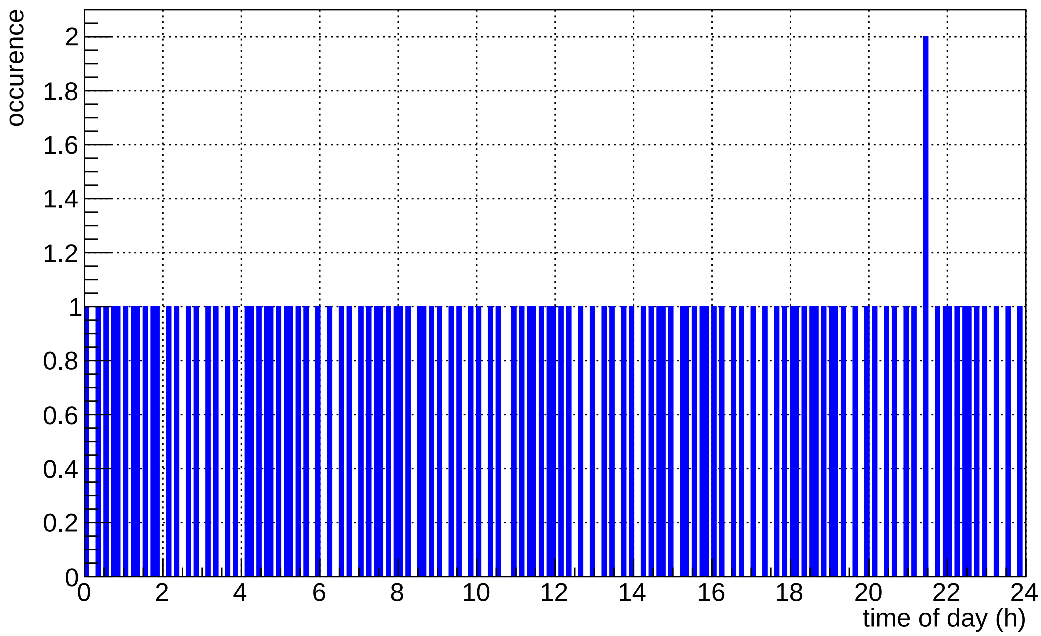

Figure 5.4.: Distribution of the starting times of run cycles for the SDS-II longterm measurement.

5.4. FPD background analyses

Several standard analyses for the FDP data have been performed, in order to investigate the background behavior of the different settings. The region of interest (ROI) for those analyses has been determined as follows. Electrons arriving at the detector are expected to have an energy of:

$$E_0 = E_i + e\left(-U_\mathrm{A} + U_\mathrm{PAE} + U_\mathrm{BIAS}\right) = 22.7\,\mathrm{keV}, \tag{5.1}$$

where $E_i \approx 0$ is the initial electron energy, $U_\mathrm{A} = -18.6\,\mathrm{kV}$ is the spectrometer voltage which accelerates electrons leaving the spectrometer towards the detector, $U_\mathrm{PAE} = 4\,\mathrm{kV}$ is the post acceleration voltage and $U_\mathrm{BIAS} = 0.12\,\mathrm{kV}$ is the bias voltage of the FPD. Accounting for the energy resolution of the detector of about 2.2 keV (FWHM), the electron ROI is defined as 19.7 to 24.7 keV.

An overview of the background characteristics of setting 1 is displayed in Figure 5.5. In (a), the pixel distribution can be seen, which in this case images about 120 m^2 of the surface of the spectrometer vessel corresponding to a fraction of about $^1/_5$ of the whole surface. The support structure from the IE system produces a ring like structure on the pixel distribution, which is a little bit shifted to the lower right due to a slight misalignment of the detector.

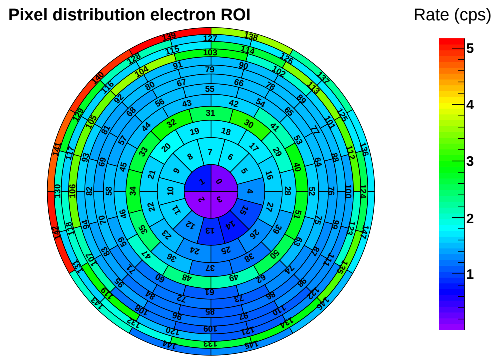

(a) Pixel distribution

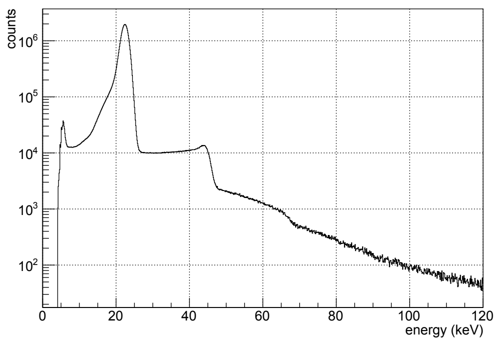

(b) Energy spectrum

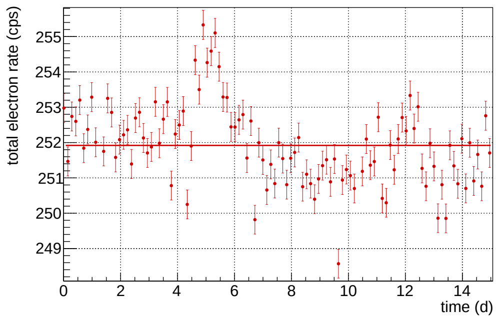

(c) Rate trend

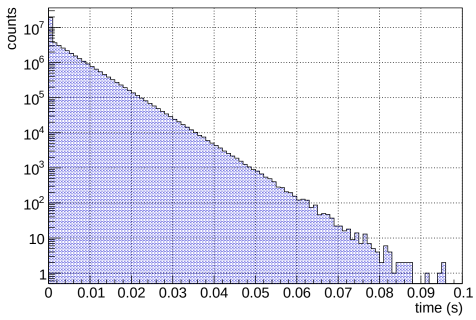

(d) Time difference spectrum

Figure 5.5.: Overview of the FPD characteristics for the asymmetric magnetic field setting (setting 1).

The energy distribution is shown in (b), where a large peak can be seen in the region of interest. Below about 7 keV, there is a steep rise due to electronic noise. Another peak like structure is visible at twice the expected electron energy. The reason for this is that two electrons hitting the same pixel within a smaller time frame than the shaping length (1.6 μs) are counted as one event with both energies summed up. This happens in case of correlated events, where more than one electron are produced at the same time, for example when a muon produces more than one secondary electron in the surface of the spectrometer. A bump at approximately three times the expected energy might be due to events with even three electrons hitting the same pixel within a very short time.

Figure 5.5c shows the rate trend for the asymmetric setting. As expected, the rate is rather high with an average value of (251.92 ± 0.04) cps. Fluctuations of up to ±1 % can be seen. A more detailed analysis of those fluctuations in comparison with the muon rate fluctuations will be given in chapter 6.

The time difference spectrum is displayed in (d). Apart from the first bin corresponding to correlated events, it shows an exponential decrease indicating a Poissonian process, i.e. the events are randomly distributed in time.

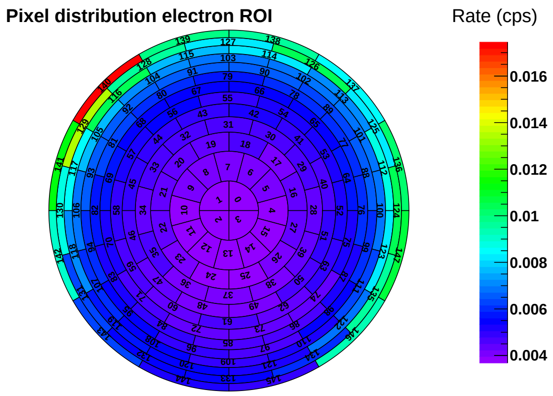

(a) Pixel distribution

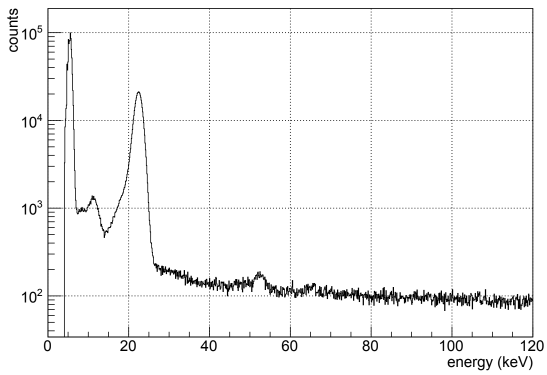

(b) Energy spectrum

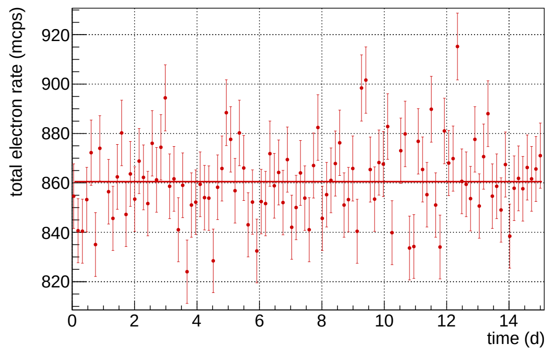

(c) Rate trend

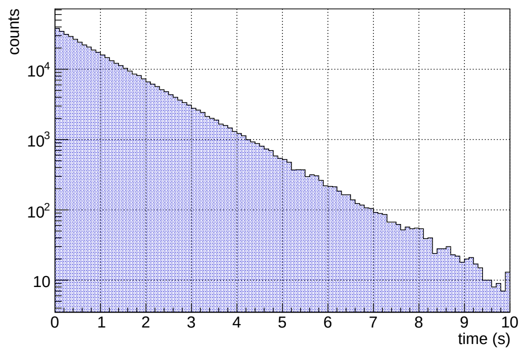

(d) Time difference spectrum

Figure 5.6.: Overview of the FPD characteristics for the symmetric magnetic field setting without electrostatic shielding (setting 2).

Figure 5.6 shows the characteristics of setting 2, hence the one with symmetric magnetic field and almost no electrostatic shielding. The pixel distribution in (a) shows a rise in the rate at higher radii indicating that background electrons are drifting into the fluxtube. There is a “hot spot” in the upper left and a “cold spot” at the bottom. So far it is not clear, where those features come from. The location of the high voltage feedthrough ports at the east side of the spectrometer fits the “hot spot”, but that could just as well be a coincidence.

In the energy spectrum, the peak in the electron ROI and the electronic noise can be seen similar to the asymmetric case, but there are two additional features visible. Below the electron ROI appears another peak that has already been observed in the first commissioning measurement phase. It has been identified to be caused by hydrogen anions from the residual gas (see [46]). Yet another small peak can be seen at energies around ≈ 53 keV, hence an initial energy of about 30 keV. It can be explained by conversion electrons from ^{210}Pb atoms and has been investigated further in [84]. The average rate for this setting accounts to (860 ± 1) mcps.

An overview of setting 3 with an IE offset of -100 V is displayed in Figure 5.7. The pixel distribution is very similar to setting 2, whereas the total rate is a little lower with an average of (692 ± 1) mcps. In the energy spectrum, the hydrogen anion peak seems to have almost vanished, instead there is an additional peak at twice the electron energy again.

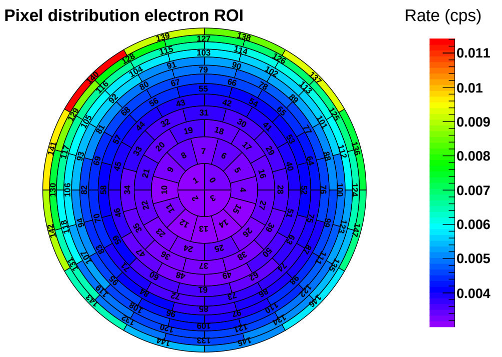

(a) Pixel distribution

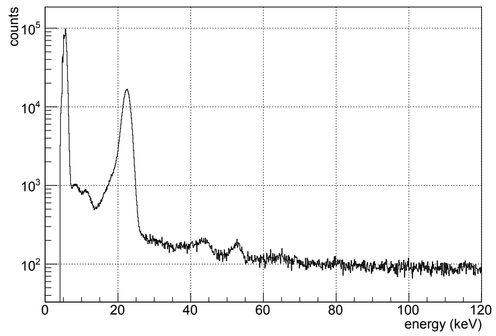

(b) Energy spectrum

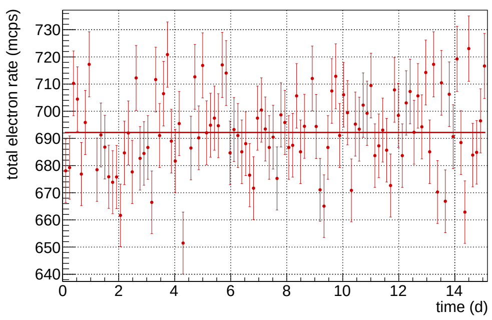

(c) Rate trend

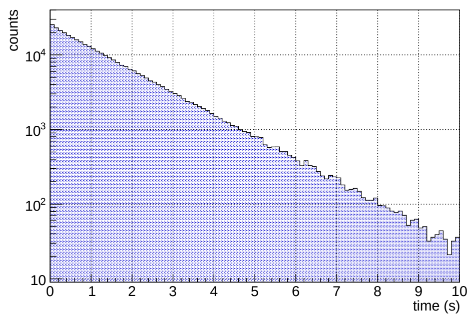

(d) Time difference spectrum

Figure 5.7.: Overview of the FPD characteristics for the symmetric magnetic field setting with an electrostatic shielding of 100 V (setting 3).

6. Correlation studies of muon induced background at the main spectrometer

In this chapter, fluctuations in the muon rate are compared to fluctuations in the background rate at the main spectrometer for the measurement described in chapter 5 in order to determine the fraction of muon induced background in the main spectrometer. The analysis strategy is described in section 6.1 and applied to the high energy region of the FPD intrinsic background in section 6.2. Results for settings 1 to 3 of the longterm measurement (see Table 5.1) are given in section 6.3 and a more detailed investigation of the asymmetric setting is presented in section 6.4. The results of additional measurements with 0 V IE offset potential are presented in section 6.5.

6.1. Analysis strategy

The analysis is based on two assumptions:

1. The spectrometer background can be split in a muon induced fluctuating background component and a time independent component of at least one other source (see Figure 6.1).

2. The muon induced background component is directly correlated with the muon rate.

Hence

$$R_{\mathrm{e}}(t) = \alpha \cdot R_{\mu}(t) + R_{\mathrm{x}}, \tag{6.1}$$

where $R_{\mathrm{e}}(t)$ is the electron rate measured at the detector, $R_{\mu}(t)$ is the muon rate, R_{x} is the rate of the time independent remaining background x and α represents the linear coefficient for the relation between muon rate and muon induced background rate.

This can be written in terms of normalized rates as follows

$$\frac{R_{\mathrm{e}}(t)}{\overline{R_{\mathrm{e}}}} = \alpha \cdot \underbrace{\frac{\overline{R_{\mu}}}{\overline{R_{\mathrm{e}}}}}_{=:a} \cdot \frac{R_{\mu}(t)}{\overline{R_{\mu}}} + \underbrace{\frac{R_{\mathrm{x}}}{\overline{R_{\mathrm{e}}}}}_{=1-a} = a \cdot \frac{R_{\mu}(t)}{\overline{R_{\mu}}} + (1-a). \tag{6.2}$$

Here, $\overline{R_{\mathrm{e}}}$ and $\overline{R_{\mu}}$ are the averaged electron and muon rate respectively. As average, the arithmetic mean was taken, hence the sum of all data points divided by the number of data points. There are three scenarios:

$\boldsymbol{a = 1}$:

The whole background is muon induced, therefore the fluctuations of the normalized muon rate and the normalized electron rate at the FPD are identical.

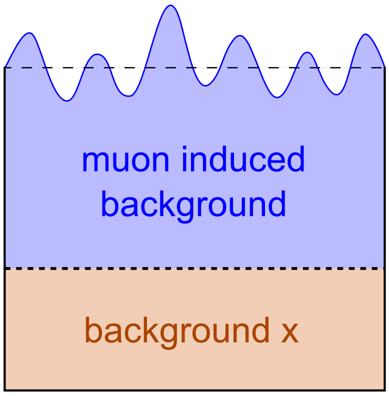

Figure 6.1.: The background at the KATRIN main spectrometer can be split into a time independent background component and a muon induced component that shows variations in time.

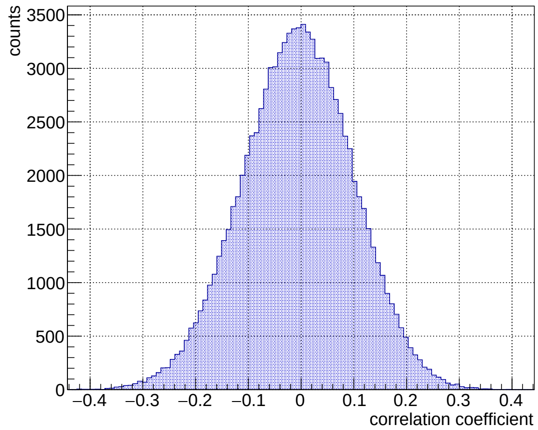

Figure 6.2.: Correlation distribution of setting 2.

$0 < a < 1$:
A fraction a of the background is muon induced and the remaining background is time independent. In this case, the fluctuations have the same shape, but the amplitude of the electron rate variations is correspondingly smaller compared to the muon rate variations.

$a = 0$:
The remaining background is not muon induced, hence no fluctuations in the electron rate at the detector are visible.

By plotting the normalized electron rate over the normalized muon rate and applying a linear fit, the fraction of muon induced background is given by the slope a. To test the linearity of the relation, the Pearson correlation coefficient has been determined (see Equation 4.4). A case resampling Monte Carlo bootstrap method [85] has been used to estimate the uncertainty of the Pearson coefficient. In order to do so, the dataset has been resampled with replacement 10000 times, each time calculating the correlation coefficient. The standard deviation from the resulting distribution has been used as an estimate for the uncertainty. As an example, the correlation distribution of setting 2 can be seen in Figure 6.2.

6.2. Correlation between muon rate and high energy region of FPD

The normalized muon rate for the whole SDS-II longterm measurement is shown in Figure 6.3, where each point corresponds to an FPD run. Modules 1 and 2 were excluded, as their rate dropped significantly in case of setting 1. This drop in rate is most likely due to a reduced efficiency of the PMTs due to the higher magnetic field at their positions.

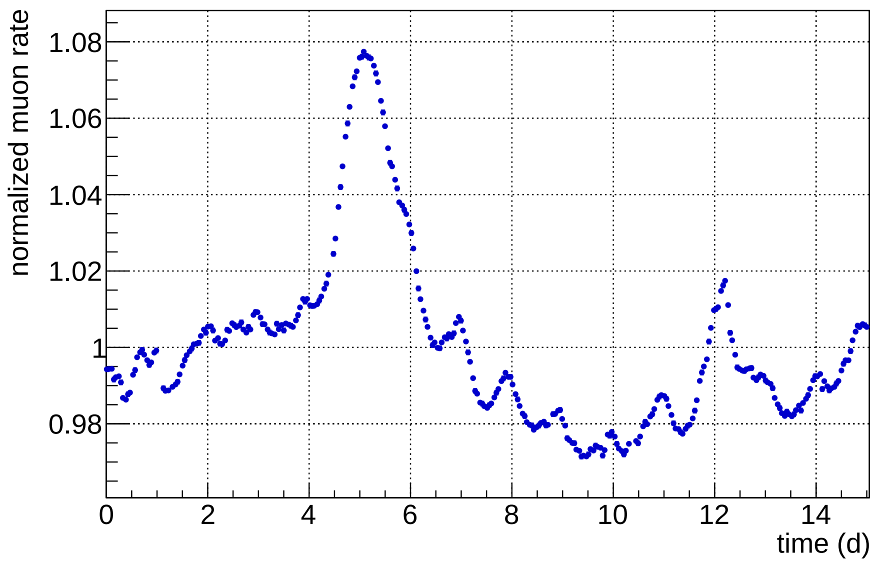

Figure 6.3.: Normalized muon rate for the SDS-II measurement. Each point corresponds to an FPD run.

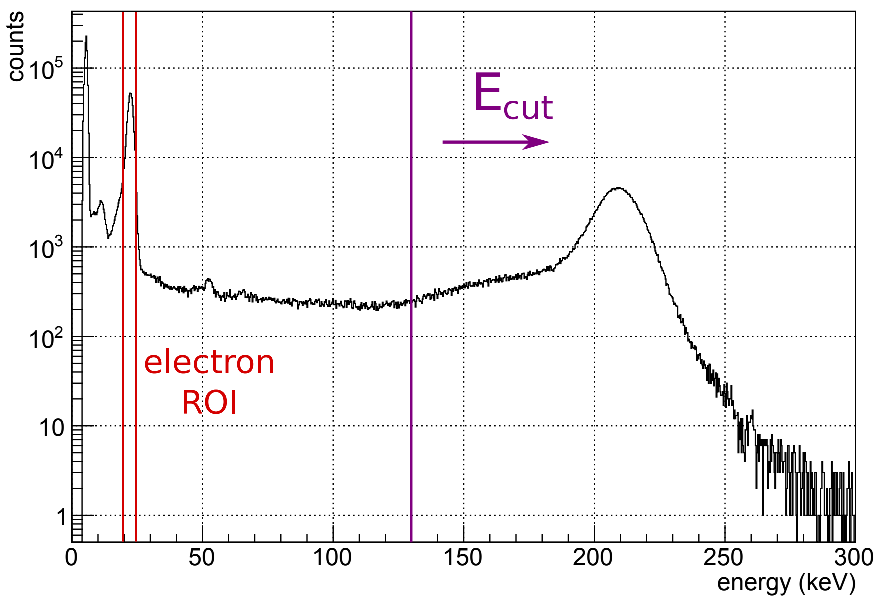

Figure 6.4.: Energy spectrum for setting 2. Above 130 keV most events are most likely due to cosmic muons crossing the detector. The usual electron ROI is shown as well.

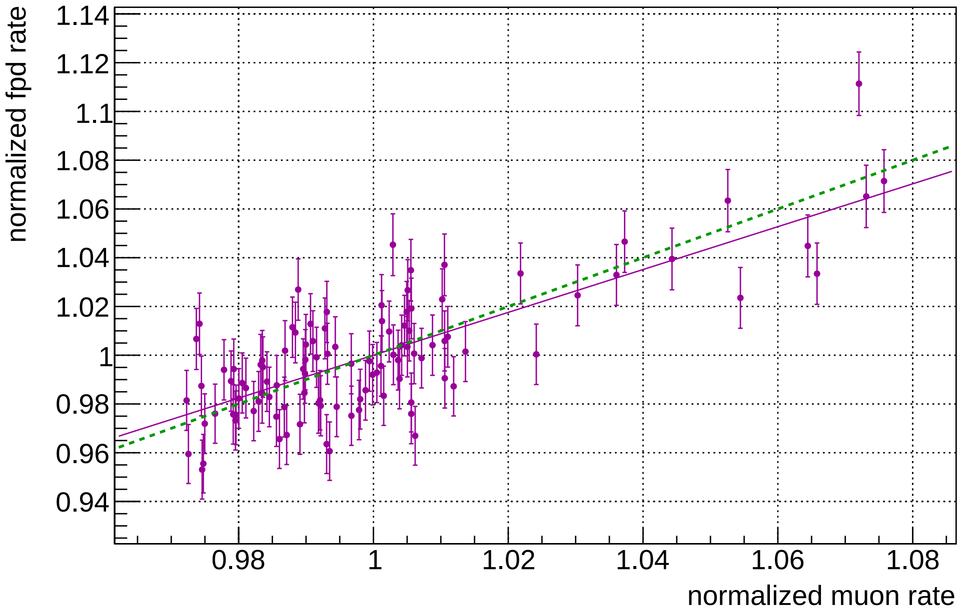

Figure 6.5.: Correlation of muon rate and high energy FPD rate. A fraction of (88 ± 5) % seems to be due to cosmic muons. The correlation corresponds to $r = 0.711 \pm 0.002$. The dashed green line corresponds to $a = 1$, i.e. completely muon induced.

The average muon rate measured with the remaining 6 large modules and the small one on top of the spectrometer is (1420.34 ± 0.03) cps. Due to a low-pressure system passing over Karlsruhe the weekend after Christmas, there was a steep rise of the muon rate corresponding to a relative variation of almost 8 %.

It is expected, that most events measured with the FPD with an energy higher than 130 keV are due to cosmic muons directly passing through the detector. An investigation of that high energy region provides a test for the above described analysis method. In Figure 6.4, the energy spectrum for setting 2 is shown up to an energy of 300 keV. At about 130 keV, a moderate rise can be seen followed by a larger peaklike structure. The peaklike structure is an artifact of the DAQ system due to events in the overflow bin. As the maximum energy is different for the 148 channels, this results in an overflow peak. The usual electron region of interest is shown too, but in this case a cut at an energy of 130 keV has been made in order to look for those events that are directly due to muons hitting the FPD.

Following the procedure described above, the normalized FPD rate in the high energy region has been plotted as a function of the normalized muon rate (Figure 6.5). Here, each point corresponds to a whole run cycle, i.e. a run of each setting. The correlation between the two rates is $r = 0.711 \pm 0.002$ and (88 ± 5) % of the high energy FPD events are due to muons running through the detector, which confirms the expectation and thus shows that the procedure works.

6.3. Correlation between muon rate and background electron rate at the FPD

Figure 6.6 shows the correlation between muon rate and electron rate for setting 1. There is a clear correlation of $r = 0.72 \pm 0.06$, but the fraction of muon induced background electrons is only (14.4 ± 0.7) %. Considering that in this particular setting the magnetic field lines guide electrons from the surface directly to the detector, it is rather unexpected, that the fraction of muon induced background is so small. Apparently there is at least one other, much stronger background source which produces electrons at the inner surface of the spectrometer.

In Figure 6.7, the correlations of settings 2 and 3 are shown. Both settings appear to have no significant correlation. Their correlation coefficients are $r = -0.01 \pm 0.11$ and $r = 0.11 \pm 0.09$ respectively. This means on the one hand, that the magnetic shielding is in fact very effective, at least for the muon induced background. On the other hand, the source of the remaining background remains unknown.

It should be noted though, that the background rate in setting 3 is not the lowest rate achievable. With a third cold baffle and a 5 G magnetic field configuration, the minimum background achieved so far is (477 ± 3) mcps. There are several ideas where the remaining background may come from. Those ideas are subject of current investigations.

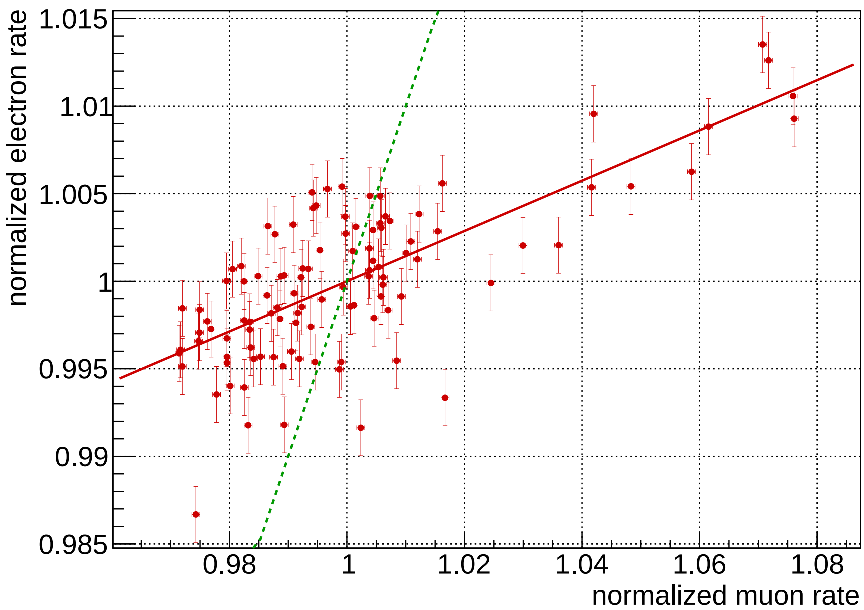

Figure 6.6.: Correlation between muon rate and electron rate at the detector for setting 1. A fraction of (14.4 ± 0.7) % of the background rate in this setting appears to be muon induced. The correlation corresponds to $r = 0.72 \pm 0.06$. The green dashed line represents the case of fully muon induced background ($a = 1$).

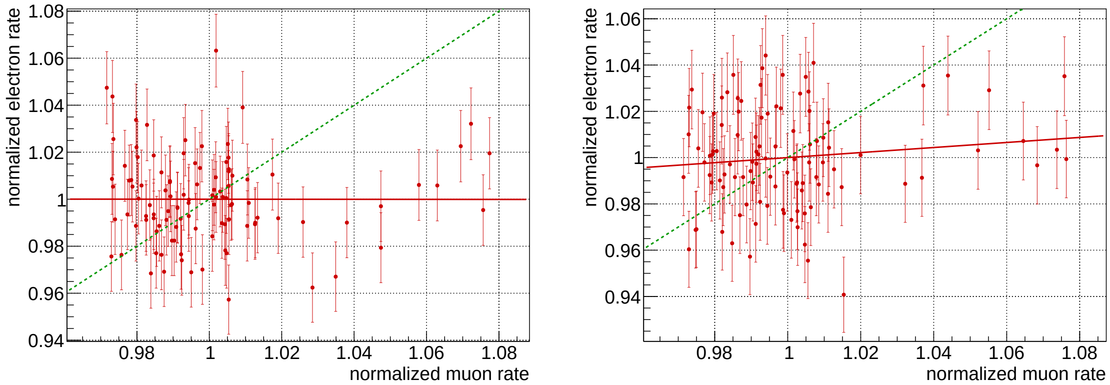

(a) Setting 2 **(b)** Setting 3

Figure 6.7.: Correlation between muon rate and electron rate at the detector for settings 2 and 3. No significant correlation can be seen in both cases. The green dashed line represents the case of fully muon induced background.

6.4. Comparison of single and cluster events for setting 1 (asymmetric magnetic field)

In order to further investigate the muon induced background, an additional selection criterion was introduced. As visualized in Figure 6.8, two or more events are considered to be in a cluster, when the time difference between them is smaller than Δt. The other events are considered to be single events. In this case, the time difference is chosen to be $\Delta t = 0.2$ ms, as that is where a kink in the time difference spectrum occurs (see Figure Figure 6.9). Using this selection criterion the background electron events of the asymmetric setting have been split into two subsets and the correlation to the muon rate has been determined.

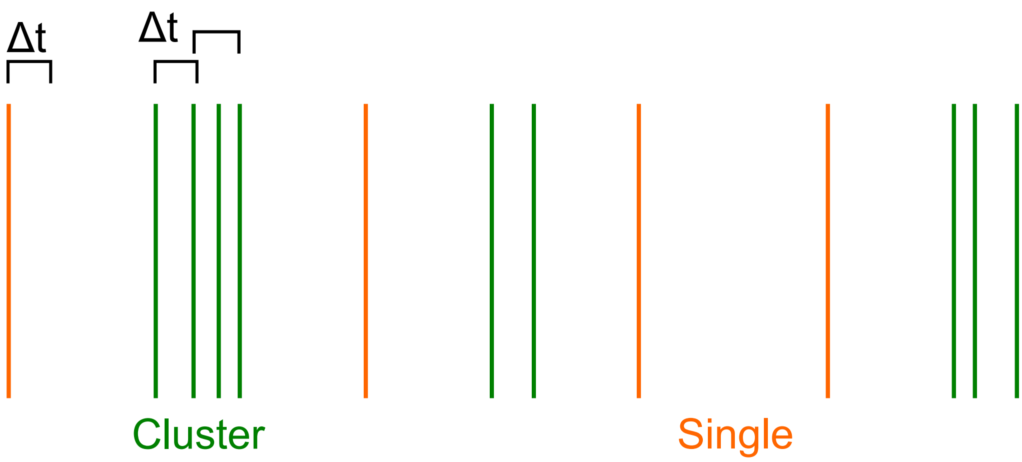

Figure 6.8.: Events are considered to be part of a cluster, if the time difference between them is smaller than a set value Δt which is $\Delta t = 0.2$ ms in this case.

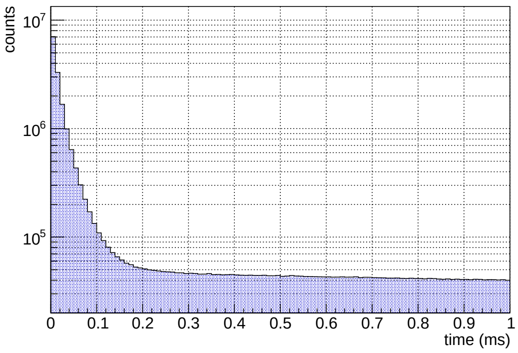

Figure 6.9.: Time difference spectrum for setting 1. Two parts can clearly be distinguished, a prompt contribution below 0.2 ms and a “slow” contribution above.

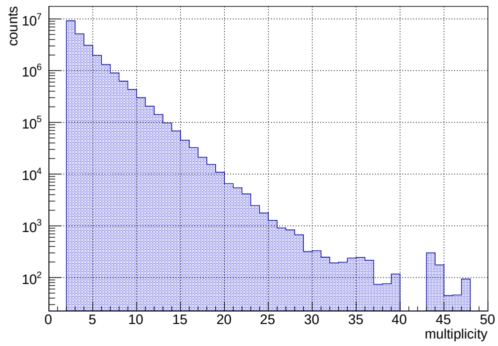

Figure 6.10.: Multiplicity of cluster events in setting 1.

In Figure 6.10, the multiplicity of the cluster events is shown. It shows an exponential decrease, but there is still a rather high contribution of high multiplicity events. In addition, high multiplicity events are systematically underestimated, as not all electrons produced in clusters reach the detector due to the magnetic mirror effect. This is further evidence for another non-muonic background source, as it is unlikely that one muon produces such a high number of electrons.

Figure 6.11 shows the correlation between muon rate and the rate of background electrons produced in clusters. With $r = 0.28 \pm 0.09$, the correlation is less pronounced than in the case of all background events. The fraction of muon induced cluster events would be (6.2 ± 0.9) %, but it is questionable to make that statement, as there is only a weak evidence for a correlation.

The correlation for the selection of single events is shown in Figure 6.12, which is with $r = 0.90 \pm 0.03$ correspondingly higher. (24 ± 1) % of single background events seem to be muon induced, which is about 10 percentage points more compared to the case where all events were considered. All results for setting 1 are summarized in Table 6.1.

The fact that the correlation is so much higher for single events than for events produced in clusters, whereas the rates are comparable indicates that most of the muon induced background is due to single events, which is in contradiction to the expectation that a muon produces more than one electron at the surface of the spectrometer.

Table 6.1.: Summary of the results for setting 1 (asymmetric setting with −5 V electrostatic shielding).

Selection	Rate (cps)	Correlation r	Slope a
All events	251.92 ± 0.04	0.72 ± 0.06	0.144 ± 0.007
Cluster events	135.38 ± 0.03	0.28 ± 0.09	0.062 ± 0.009
Single events	116.53 ± 0.03	0.90 ± 0.03	0.24 ± 0.01

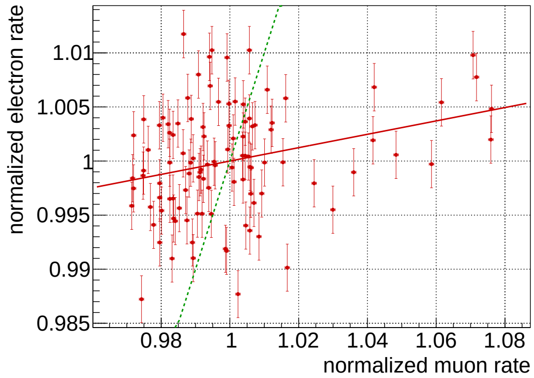

Figure 6.11.: Correlation between muon rate and electron rate at the detector for events produced in clusters in the asymmetric setting. The correlation corresponds to only $r = 0.28 \pm 0.09$.

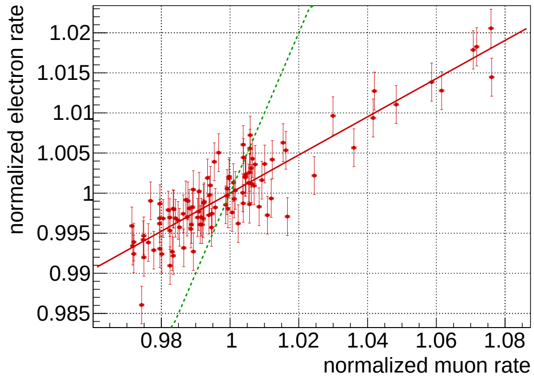

Figure 6.12.: Correlation between muon rate and electron rate at the detector for single events in the asymmetric setting. There is a clear correlation of $r = 0.90 \pm 0.03$ and the fraction of muon induced single events is $(24 \pm 1)\,\%$.

However, it should be noted that the inner electrode shields electrons with an energy less than 5 eV. As the secondary electrons from cosmic muons are expected to have very low energies, it is not unlikely that already a large part of the muon induced background is reflected back to the spectrometer wall by this low offset. Also, as mentioned above, only a fraction of the secondaries is detected, as some of the electrons are reflected due to magnetic mirror effect as they travel from the spectrometer towards the increasing magnetic field of the pinch magnet. Therefore it can happen, that electrons that were actually produced in a cluster are identified as single electrons when their "partners" escape detection.

6.5. Measurement without electrostatic shielding

As a supplement to the longterm measurement, a measurement with four different magnetic field configurations has been performed, where the inner electrode was connected to vessel potential in order to turn the electrostatic shielding off. Setting 4 was the same asymmetric magnetic field setting as before, whereas settings 5 to 7 were symmetric magnetic field settings with 3.8 G, 5 G and 9 G respectively.

Table 6.2.: Background electron rates for symmetric settings 5 to 7 without electrostatic shielding.

Setting	Magnetic field	Rate (mcps)
5	3.8 G	926 ± 5
6	5.0 G	670 ± 4
7	9.0 G	362 ± 3

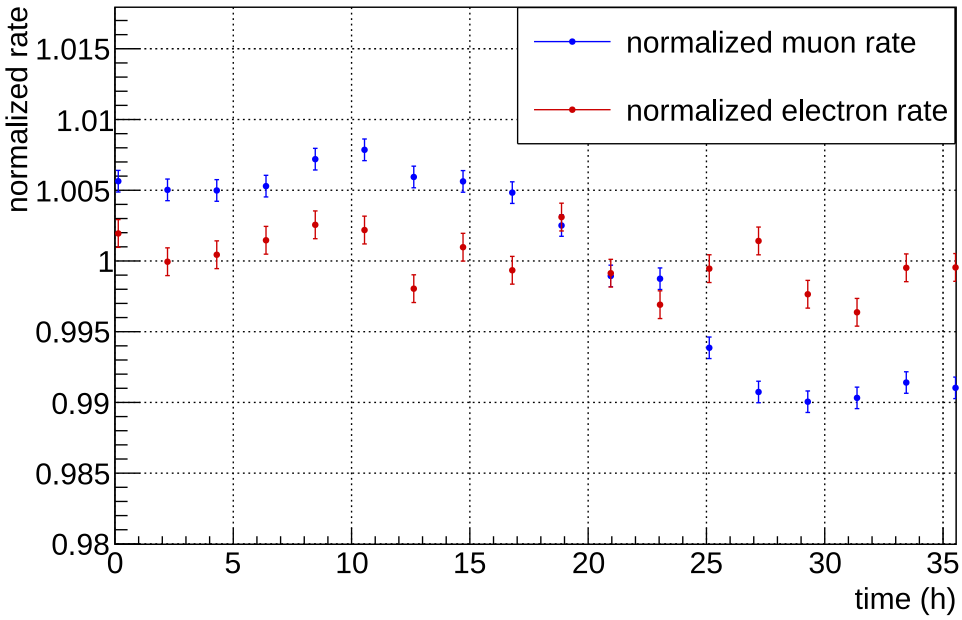

Figure 6.13.: Normalized muon (blue) and electron rate (red) over time for the asymmetric setting without electrostatic shielding. Both rates show only a small variation of less than ±1 %.

The post acceleration electrode was set to $U_{\text{PAE}} = 10\,\text{kV}$ and the vessel potential was $U_{\text{A}} = -18.6\,\text{kV}$, resulting in an expected electron energy of $E_0 = 28.7\,\text{keV}$ (see Equation 5.1). Hence, the electron ROI is defined as 25.7 keV to 30.7 keV.

The measurement lasted for 1.5 days. However, no major fluctuations of the muon flux were observed during this time which makes a correlation study difficult. The rates of settings 5 to 7 are listed in Table 6.2. Figure 6.13 shows the normalized muon and electron rate over time for setting 4. Their correlation is shown in Figure 6.14 and accounts to $r = 0.5 \pm 0.2$.

An analysis of cluster and single events has been performed, the results are summarized in Table 6.3. In comparison to the measurement with −5 V IE offset, the fraction of muon induced single events did not change significantly, but there seem to be a lot more muon induced secondaries produced in clusters, as both their rate and the fraction increased significantly. A viable explanation seems to be that muon induced secondaries produced in clusters are very low energetic, as a large part of them are already reflected back to the spectrometer wall by a −5 V offset potential. This is in good agreement with the expectation of very low energetic true secondaries [66].

Table 6.3.: Summary of the results of setting 4 (asymmetric magnetic field with no electrostatic shielding).

Selection	Rate (cps)	Correlation r	Slope a
All events	869.0 ± 0.2	0.5 ± 0.2	0.15 ± 0.08
Cluster events	589.4 ± 0.2	0.3 ± 0.2	0.14 ± 0.04
Single events	209.6 ± 0.1	0.5 ± 0.1	0.26 ± 0.07

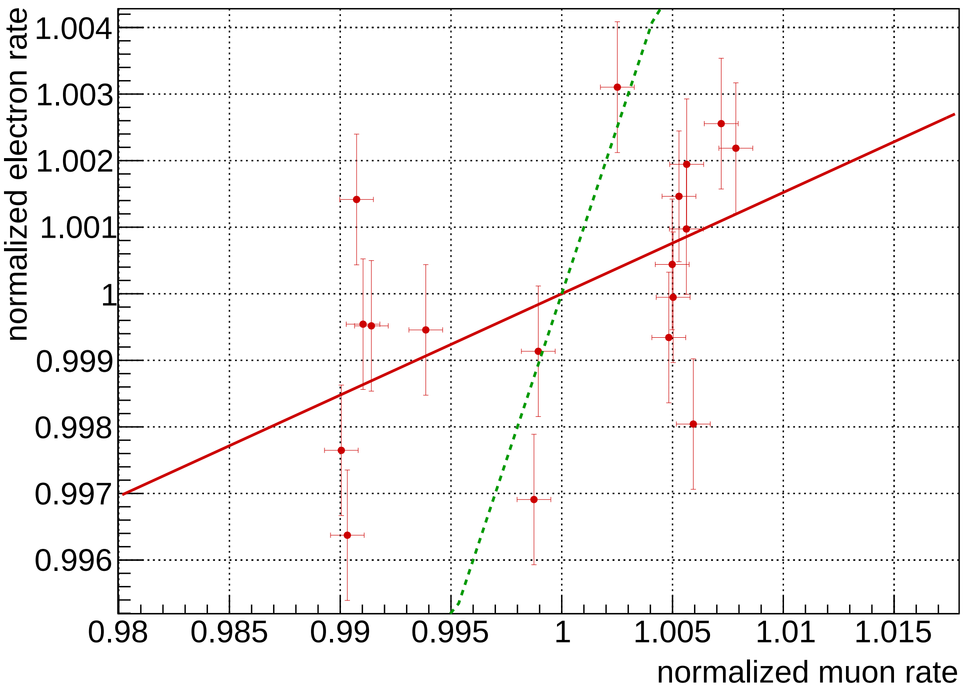

Figure 6.14.: Correlation of muon rate and background electron rate for setting 4 (asymmetric magnetic field): $r = 0.5 \pm 0.2$. In this configuration, (15 ± 8) % of the background appears to be muon induced. The dashed green line corresponds to 100 % muon induced background.

7. Conclusion

Since the discovery of neutrino oscillations proved that neutrinos are massive particles it has been of great interest to determine the absolute mass scale of the neutrinos. The KATRIN experiment is a next-generation direct neutrino mass experiment aiming to determine the mass of the electron antineutrino through an investigation of tritium β-decay kinematics with a sensitivity of 200 meV/c^2 (90 % C.L.). Such a high sensitivity requires a very low background level of 10 mcps. Therefore a good understanding of the background sources and the development of countermeasures to reduce the background is of great importance.

Predecessor experiments with spectrometers of MAC-E filter type showed that cosmic muons produce secondary electrons as they pass through the spectrometer wall. Within this thesis, the cosmic muon induced background at the KATRIN main spectrometer has been investigated. The muon rate at sea level shows fluctuations in time which depend on atmospheric and solar parameters. Those fluctuations can be used to gain a better understanding of the connection between cosmic muons and the background rate at the main spectrometer by investigating the correlation between the fluctuations of the muon rate and those of the background electron rate.

The muon detector system was operated for three months in a standalone mode in preparation of the correlation measurements. During this time, relative fluctuations of the muon flux of ±3.5 % were observed. The correlation of those fluctuations to variations in atmospheric pressure and temperature has been investigated. A relatively high correlation of $r = -0.64$ to the atmospheric pressure was found, whereas the correlation to the temperature was less pronounced. A diurnal variation of the muon flux connected to a modulation in the primary cosmic ray flux was also observed.

In order to investigate the muon induced background component of the main spectrometer, an important longterm measurement has been performed as part of the second SDS commissioning phase with the muon detector system running in parallel. It contained measurements with both asymmetric and symmetric magnetic field configurations and different inner electrode offsets. An analysis strategy for correlation studies has been developed to determine the contribution of the muon induced background component in the main spectrometer.

In the asymmetric magnetic field configuration, the field lines directly guide electrons from about $^1\!/_5$ of the spectrometer surface to the detector. Still, only a fraction of $\approx$ 15 % of the secondary electrons appears to be muon induced. For a more detailed investigation, the data has been split in single and cluster events by a cut on the time difference between events. The results indicate that the main part of muon induced true secondaries produced in clusters is very low energetic ($<$ 5 eV), which is in good agreement with the expectation from the literature. In case of the symmetric magnetic field configuration, no significant correlation to the muon rate could be found. On the upside, this means that the magnetic shielding is very effective at least for the muon induced background. However, it also means that the source of the remaining background is still unknown.

It can be concluded, that the muon induced background is not as dominant as previously assumed, most of the muon induced secondary electrons are reflected back to the wall by the magnetic and electrostatic shielding mechanisms. Future background investigations will focus on finding the source(s) of the remaining background. However, the muon induced background might become of interest again once the background is reduced to a lower level.

Appendix

A. High voltage settings and DAQ channel assignment for the muon system

Table A.1.: High voltage settings and DAQ channel assignments for the muon modules. Module 9 is the small one on top of the spectrometer. Modules 1-5 and 6-8 are supplied by separate HV devices at the west and east side of the spectrometer respectively. Module 9 is connected to a small portable HV device with one channel.

	HV		**DAQ**	
Module	Channel	Voltage	Card	Channel
1A	W0	1550	3	0
1B	W1	1550	3	14
2A	W2	1500	3	3
2B	W3	1600	3	7
3A	W4	1500	6	0
3B	W5	1500	6	14
4A	W6	1500	6	3
4B	W7	1500	6	7
5A	W8	1500	6	9
5B	W9	1500	6	23
6A	E6	1600	9	0
6B	E1	1500	9	14
7A	E2	1500	9	3
7B	E3	1500	9	7
8A	E4	1500	9	9
8B	E5	1500	9	23
9a	1	1600	3	9
9b	1	1600	3	23

B. Asymmetric magnetic field setting

The following current values have been used for the LFCS in order to create an asymmetric magnetic field.

Table B.1.: LFCS currents for the asymmetric magnetic field setting used in the SDS-II longterm measurement.

LFCS #	1	2	3	4	5	6	7	8	9	10	11	12	13	14
Current (A)	-100	-100	-50	20	20	50	60	60	40	30	0	0	0	0

C. Orca Script

The following script has been used to automatically cycle through three different electromagnetic settings of the SDS system.

```
//Name:OrcaScript
//Comments:periodically repeats 3 measurement settings:
//-asymmetric magnetic field, no inner electrode offset
//-symmetric magnetic field, no inner electrode offset
//-symmetric magnetic field, 100V inner electrode offset,
//steep cones on vessel potential
//#import "~/katrin/ORCARunControlSDS2/libs/SDS2.lib"
#import "~/katrin/ORCARunControlSDS2/libs/SDS2_ADEI.lib"
#import "~/katrin/ORCARunControlSDS2/libs/SDS2_AirCoils.lib"
#import "~/katrin/ORCARunControlSDS2/libs/SDS2_HV.lib"
#import "~/katrin/ORCARunControlSDS2/libs/SDS2_Detector_new.lib"
#import "~/katrin/ORCARunControlSDS2/libs/SDS2_RunControl.lib"
#import "~/katrin/ORCARunControlSDS2/libs/SDS2_Egun.lib"

function setBFieldAsym() {
  array asymPolarities[16] = {1.0 ,1.0, 1.0, 0.0, 0.0, 0.0,
      0.0, 0.0, 0.0, 0.0, 0.0, 0.0, 0.0, 0.0, 0.0, 0.0};
  array asymCurrents[14] = {100.0 ,100.0 ,50.0, 20.0, 20.0,
      50.0, 60.0, 60.0, 40.0, 30.0, 0.0, 0.0, 0.0, 0.0};
  turnOffLFCS();
  queueAirCoilPolarities(asymPolarities);
  sleep(10);
  queueLFCSCurrents(asymCurrents);
  sleep(20);
}

function setBFieldSym() {
  array symPolarities[16] = {0.0 ,0.0, 0.0, 0.0, 0.0, 0.0,
      0.0, 0.0, 0.0, 0.0, 0.0, 0.0, 0.0, 0.0, 0.0, 0.0};
  turnOffLFCS();
  sleep(10);
  queueAirCoilPolarities(symPolarities);
  sleep(10);
  setLFCSSetting(3.8);
  sleep(20);
}

function main() {

  asymRunTime = 1500;
```

```
  symRunTime = 5000;
  flag = "online";

  print("Merry Christmas!");

  //setPAEVoltage(4000);

  do {
    //asym setting
    print("setting asymmetric configuration");
    setBFieldAsym();
    setVoltageSteepCones( 2.0 );
    setVoltageInnerElectrodeCommon( 5.0 );
    setVoltageVessel( 18600.0 );
    sleep(20);
    takeRun(asymRunTime,flag);

    //sym setting
    print("setting symmetric configuration");
    setBFieldSym();
    takeRun(symRunTime,flag);
    print("changing IE potential");
    setVoltageInnerElectrodeCommon( 100.0 );
    setVoltageVessel( 18500.0 );
    setVoltageSteepCones( 97.0 );
    sleep(20);
    takeRun(symRunTime,flag);

  } while(1);

}
```

D. FPD runs of longterm background measurement

The SDS-II longterm background measurement started with FPD run #21426 on the 22nd of December 2014 and ended on the 6th of January 2015 with run #21749. The following runs had to be excluded mainly due to lost SlowControl set points:

#21448 baffle 3 started warming up

#21449 baffle 3 warm-up

#21453 lost set point for air coil polarity → wrong HV configuration

#21521 lost set point for vessel voltage → wrong vessel voltage

#21614 lost set point for HV power supply E15 → wrong HV configuration

#21648 lost set point for HV power supply E2 and W2 → wrong HV configuration

#21649 lost set point for HV power supply E2 and W2 → wrong HV configuration

List of Figures

List of Tables

Bibliography

[1] J. Chadwick. "The intensity distribution in the magnetic spectrum of beta particles from radium (B + C)". In: *Verh.Phys.Gesell.* 16 (1914), pp. 383–391.

[2] W.E.F. Pauli, R. Kronig, and V.F. Weisskopf. *Collected scientific papers.* Offener Brief an die Gruppe der Radioaktiven bei der Gauvereinstagung zu Tübingen (datiert 4. Dez. 1930). New York, NY: Interscience, 1964.

[3] C.L. Cowan et al. "Detection of the free neutrino: A Confirmation". In: *Science* 124 (1956), pp. 103–104. DOI: 10.1126/science.124.3212.103.

[4] G. Danby et al. "Observation of High-Energy Neutrino Reactions and the Existence of Two Kinds of Neutrinos". In: *Phys.Rev.Lett.* 9 (1962), pp. 36–44. DOI: 10.1103/PhysRevLett.9.36.

[5] K. Kodama et al. "Observation of tau neutrino interactions". In: *Phys.Lett.* B504 (2001), pp. 218–224. DOI: 10.1016/S0370-2693(01)00307-0. arXiv: hep-ex/0012035 [hep-ex].

[6] Pushpalatha C. Bhat. "Observation of a Higgs-like Boson in CMS at the LHC". In: *Nucl.Phys.Proc.Suppl.* 234 (2013), pp. 7–14. DOI: 10.1016/j.nuclphysbps.2012.11.003.

[7] Georges Aad et al. "Observation of a new particle in the search for the Standard Model Higgs boson with the ATLAS detector at the LHC". In: *Phys.Lett.* B716 (2012), pp. 1–29. DOI: 10.1016/j.physletb.2012.08.020. arXiv: 1207.7214 [hep-ex].

[8] V.M. Lobashev. "The search for the neutrino mass by direct method in the tritium beta-decay and perspectives of study it in the project KATRIN". In: *Nucl.Phys.* A719 (2003), pp. 153–160. DOI: 10.1016/S0375-9474(03)00985-0.

[9] C. Kraus et al. "Final results from phase II of the Mainz neutrino mass search in tritium β decay". In: *The European Physical Journal C - Particles and Fields* 40.4 (2005), pp. 447–468. DOI: 10.1140/epjc/s2005-02139-7.

[10] Marco Kleesiek. "A Data-Analysis and Sensitivity-Optimization Framework for the KATRIN Experiment". PhD thesis. Karlsruher Institut für Technologie (KIT), 2014. URL: http://digbib.ubka.uni-karlsruhe.de/volltexte/1000043301.

[11] B. Pontecorvo. "Inverse beta-processes and non-conservation of lepton charge". In: (1957).

[12] B. Pontecorvo. "Neutrino Experiments and the Problem of Conservation of Leptonic Charge". In: *Sov.Phys.JETP* 26 (1968), pp. 984–988.

[13] John N. Bahcall and M.H. Pinsonneault. “Standard solar models, with and without helium diffusion and the solar neutrino problem”. In: *Rev.Mod.Phys.* 64 (1992), pp. 885–926. DOI: 10.1103/RevModPhys.64.885.

[14] R. Davis. “A review of the Homestake solar neutrino experiment”. In: *Prog.Part.Nucl.Phys.* 32 (1994), pp. 13–32. DOI: 10.1016/0146-6410(94)90004-3.

[15] Q.R. Ahmad et al. “Direct evidence for neutrino flavor transformation from neutral current interactions in the Sudbury Neutrino Observatory”. In: *Phys.Rev.Lett.* 89 (2002), p. 011301. DOI: 10.1103/PhysRevLett.89.011301. arXiv: nucl-ex/0204008 [nucl-ex].

[16] G. Bellini et al. “Neutrinos from the primary proton-proton fusion process in the Sun”. In: *Nature* 512.7515 (2014), pp. 383–386. DOI: 10.1038/nature13702.

[17] John N. Bahcall, Aldo M. Serenelli, and Sarbani Basu. “New solar opacities, abundances, helioseismology, and neutrino fluxes”. In: *Astrophys.J.* 621 (2005), pp. L85–L88. DOI: 10.1086/428929. arXiv: astro-ph/0412440 [astro-ph].

[18] Ziro Maki, Masami Nakagawa, and Shoichi Sakata. “Remarks on the unified model of elementary particles”. In: *Prog.Theor.Phys.* 28 (1962), pp. 870–880. DOI: 10.1143/PTP.28.870.

[19] M.C. Gonzalez-Garcia and Yosef Nir. “Neutrino masses and mixing: Evidence and implications”. In: *Rev.Mod.Phys.* 75 (2003), pp. 345–402. DOI: 10.1103/RevModPhys.75.345. arXiv: hep-ph/0202058 [hep-ph].

[20] Y. Fukuda et al. “Evidence for oscillation of atmospheric neutrinos”. In: *Phys.Rev.Lett.* 81 (1998), pp. 1562–1567. DOI: 10.1103/PhysRevLett.81.1562. arXiv: hep-ex/9807003 [hep-ex].

[21] R. Acquafredda et al. “The OPERA experiment in the CERN to Gran Sasso neutrino beam”. In: *JINST* 4 (2009), P04018. DOI: 10.1088/1748-0221/4/04/P04018.

[22] P. Adamson et al. “Measurement of the neutrino mass splitting and flavor mixing by MINOS”. In: *Phys.Rev.Lett.* 106 (2011), p. 181801. DOI: 10.1103/PhysRevLett.106.181801. arXiv: 1103.0340 [hep-ex].

[23] Ahn, M.H. et al. (K2K Collaboration). “Measurement of neutrino oscillation by the K2K experiment”. In: *Physical Review D* 74 (7 2006), p. 072003. DOI: 10.1103/PhysRevD.74.072003.

[24] W. Hampel et al. “GALLEX solar neutrino observations: Results for GALLEX IV”. In: *Phys.Lett.* B447 (1999), pp. 127–133. DOI: 10.1016/S0370-2693(98)01579-2.

[25] J.N. Abdurashitov et al. “Solar neutrino flux measurements by the Soviet-American Gallium Experiment (SAGE) for half the 22 year solar cycle”. In: *J.Exp.Theor.Phys.* 95 (2002), pp. 181–193. DOI: 10.1134/1.1506424. arXiv: astro-ph/0204245 [astro-ph].

[26] M. Altmann et al. “Complete results for five years of GNO solar neutrino observations”. In: *Phys.Lett.* B616 (2005), pp. 174–190. DOI: 10.1016/j.physletb.2005.04.068. arXiv: hep-ex/0504037 [hep-ex].

[27] Abe, S. et al. (KamLAND Collaboration). "Precision Measurement of Neutrino Oscillation Parameters with KamLAND". In: *Physical Review Letters* 100 (2008), p. 221803. DOI: 10.1103/PhysRevLett.100.221803.

[28] F.P. An et al. "Improved Measurement of Electron Antineutrino Disappearance at Daya Bay". In: *Chin.Phys.* C37 (2013), p. 011001. DOI: 10.1088/1674-1137/37/1/011001. arXiv: 1210.6327 [hep-ex].

[29] Abe, Y. et al. (Double Chooz Collaboration). "Reactor $\overline{\nu}_e$ disappearance in the Double Chooz experiment". In: *Physical Review D* 86 (5 2012), p. 052008. DOI: 10.1103/PhysRevD.86.052008.

[30] Ahn, J. K. et al. (RENO Collaboration). "Observation of Reactor Electron Antineutrinos Disappearance in the RENO Experiment". In: *Physical Review Letters* 108 (19 2012), p. 191802. DOI: 10.1103/PhysRevLett.108.191802.

[31] KATRIN collaboration. "KATRIN Design Report". In: *FZKA scientific report* 7090 (2005). URL: http://bibliothek.fzk.de/zb/berichte/FZKA7090.pdf.

[32] E. Fermi. "Versuch einer Theorie der β-Strahlen." In: *Zeitschrift für Physik* 88.3–4 (1934), pp. 161–177. DOI: 10.1007/BF01351864.

[33] L. Gastaldo et al. "The Electron Capture ^{163}Ho Experiment ECHo: an overview". In: *J.Low Temp.Phys.* 176.5-6 (2014), pp. 876–884. DOI: 10.1007/s10909-014-1187-4. arXiv: 1309.5214 [physics.ins-det].

[34] J.A. Formaggio. "Project 8: Using Radio-Frequency Techniques to Measure Neutrino Mass". In: *Nucl.Phys.Proc.Supl.* 229-232 (2012), pp. 371–375. DOI: 10.1016/j.nuclphysbps.2012.09.058. arXiv: 1101.6077 [nucl-ex].

[35] Magnus Schlösser. "Accurate calibration of the Raman system for the Karlsruhe Tritium Neutrino Experiment". PhD thesis. Karlsruher Institut für Technologie (KIT), 2013.

[36] Steven R. Elliott and Petr Vogel. "Double beta decay". In: *Ann.Rev.Nucl.Part.Sci.* 52 (2002), pp. 115–151. DOI: 10.1146/annurev.nucl.52.050102.090641. arXiv: hep-ph/0202264 [hep-ph].

[37] Ettore Majorana. "Theory of the Symmetry of Electrons and Positrons". In: *Nuovo Cim.* 14 (1937), pp. 171–184. DOI: 10.1007/BF02961314.

[38] Stefan. Schonert. "Status of the GERmanium Detector Array (GERDA) for the search of neutrinoless beta beta decays of Ge-76 at LNGS". In: *Prog.Part.Nucl.Phys.* 57 (2006), pp. 241–250. DOI: 10.1016/j.ppnp.2005.12.006.

[39] Monica Sisti. "From Cuoricino to CUORE: Investigating neutrino properties with double beta decay". In: *J.Phys.Conf.Ser.* 203 (2010), p. 012069. DOI: 10.1088/1742-6596/203/1/012069.

[40] E. Aguayo et al. "The Majorana experiment". In: *AIP Conf.Proc.* 1417 (2011), pp. 95–99. DOI: 10.1063/1.3671044.

[41] G. Beamson, H.Q. Porter, and D.W. Turner. “The collimating and magnifying properties of a superconducting field photoelectron spectrometer”. In: *Journal of Physics E: Scientific Instruments* 13.1 (1980), p. 64. DOI: 10.1088/0022-3735/13/1/018.

[42] V.M. Lobashev and P.E. Spivak. “A method for measuring the electron antineutrino rest mass”. In: *Nuclear Instruments and Methods in Physics Research Section A: Accelerators, Spectrometers, Detectors and Associated Equipment* 240.2 (1985), pp. 305–310. DOI: 10.1016/0168-9002(85)90640-0.

[43] A. Picard et al. “A solenoid retarding spectrometer with high resolution and transmission for keV electrons”. In: *Nuclear Instruments and Methods in Physics Research Section B: Beam Interactions with Materials and Atoms* 63.3 (1992), pp. 345–358. DOI: 10.1016/0168-583X(92)95119-C.

[44] M. Babutzka et al. “Monitoring of the operating parameters of the KATRIN Windowless Gaseous Tritium Source”. In: *New Journal of Physics* 14.10 (2012), p. 103046. DOI: 10.1088/1367-2630/14/10/103046.

[45] S. Grohmann et al. “Precise temperature measurement at 30 K in the KATRIN source cryostat”. In: *Cryogenics* 51.8 (2011), pp. 438–445. DOI: 10.1016/j.cryogenics.2011.05.001.

[46] Johannes S. Schwarz. “The Detector System of the KATRIN Experiment - Implementation and First Measurements with the Spectrometer”. PhD thesis. Karlsruher Institut für Technologie (KIT), 2014. URL: http://nbn-resolving.org/urn:nbn:de:swb:90-427724.

[47] Andreas Kosmider. “Tritium Retention Techniques in the KATRIN Transport Section and Commissioning of its DPS2-F Cryostat”. PhD thesis. Karlsruher Institut für Technologie (KIT), 2012. URL: http://digbib.ubka.uni-karlsruhe.de/volltexte/1000028959.

[48] W. Gil et al. “The Cryogenic Pumping Section of the KATRIN Experiment”. In: *IEEE Transactions on Applied Superconductivity* 20.3 (2010), pp. 316–319. DOI: 10.1109/TASC.2009.2038581.

[49] Nancy Wandkowsky. “Study of background and transmission properties of the KATRIN spectrometers”. PhD thesis. Karlsruher Institut für Technologie (KIT), 2013. URL: http://digbib.ubka.uni-karlsruhe.de/volltexte/1000036631.

[50] Florian Habermehl. “Electromagnetic Measurements with the KATRIN Pre-Spectrometer”. PhD thesis. Universität Karlsruhe (TH), 2009. URL: http://digbib.ubka.uni-karlsruhe.de/volltexte/1000013549.

[51] Florian M. Fränkle. “Background Investigations of the KATRIN Pre-Spectrometer”. PhD thesis. Karlsruher Institut für Technologie (KIT), 2010. URL: http://nbn-resolving.org/urn:nbn:de:swb:90-193929.

[52] Björn Hillen. “Untersuchung von Methoden zur Unterdrückung des Spektrometeruntergrunds beim KATRIN Experiment”. PhD thesis. Westfälische Wilhelms-Universität Münster, 2011. URL: http://nbn-resolving.de/urn:nbn:de:hbz:6-22429660310.

[53] Mathias Prall. “Background Reduction of the KATRIN Spectrometers: Transmission Function of the Pre-Spectrometer and Systematic Test of the Main-Spectrometer Wire Electrode”. PhD thesis. Westfälische Wilhelms-Universität Münster, 2011. URL: http://www.researchgate.net/publication/238418212_Transmission_Function_of_the_Pre-Spectrometer_and_Systematic_Tests_of_the_Main-Spectrometer_Wire_Electrode_%28PHD_thesis%29.

[54] F. Glück et al. “Electromagnetic design of the large-volume air coil system of the KATRIN experiment”. In: *New Journal of Physics* 15.8 (2013), p. 083025. DOI: 10.1088/1367-2630/15/8/083025.

[55] J. Wolf et al. “Investigation of turbo-molecular pumps in strong magnetic fields”. In: *Vacuum* 86.4 (2011), pp. 361–369. DOI: 10.1016/j.vacuum.2011.07.063.

[56] X. Luo et al. “KATRIN NEG pumping concept investigation”. In: *Vacuum* 81.6 (2007), pp. 777–781. DOI: 10.1016/j.vacuum.2005.11.053.

[57] M. Prall et al. “A Contact-Less 2-Dimensional Laser Sensor for 3-Dimensional Wire Position and Tension Measurements”. In: *IEEE Transactions on Nuclear Science* 57.2 (2010), pp. 787–792. DOI: 10.1109/TNS.2010.2042612.

[58] M. Erhard et al. “High-voltage monitoring with a solenoid retarding spectrometer at the KATRIN experiment”. In: *Journal of Instrumentation* 9.6 (2014), P06022. DOI: 10.1088/1748-0221/9/06/P06022.

[59] Stephan Bauer. “Energy calibration and stability monitoring of the KATRIN experiment”. PhD thesis. Westfälische Wilhelms-Universität Münster, 2014. URL: http://nbn-resolving.de/urn:nbn:de:hbz:6-04329567651.

[60] J.F. Amsbaugh et al. “Focal-plane detector system for the {KATRIN} experiment”. In: *Nuclear Instruments and Methods in Physics Research Section A: Accelerators, Spectrometers, Detectors and Associated Equipment* 778.0 (2015), pp. 40 –60. ISSN: 0168-9002. DOI: http://dx.doi.org/10.1016/j.nima.2014.12.116. URL: http://www.sciencedirect.com/science/article/pii/S0168900215000236.

[61] Michelle L. Leber. “Monte Carlo Calculations of the Intrinsic Detector Backgrounds for the Karlsruhe Tritium Neutrino Experiment”. PhD thesis. University of Washington, 2010. URL: http://www.npl.washington.edu/sites/default/files/webfiles/theses/MLL_Thesis.pdf.

[62] F.M. Fränkle et al. “Radon induced background processes in the KATRIN pre-spectrometer”. In: *Astroparticle Physics* 35.3 (2011), pp. 128–134. DOI: 10.1016/j.astropartphys.2011.06.009.

[63] Stefan Görhardt. “Background Reduction Methods and Vacuum Technology at the KATRIN Spectrometers”. PhD thesis. Karlsruher Institut für Technologie (KIT), 2014. URL: http://digbib.ubka.uni-karlsruhe.de/volltexte/1000038050.

[64] Florian Müller. "Efficiency Studies of the Background Suppression by a Liquid-Nitrogen Cooled Baffle System in the KATRIN Experiment". Master's Thesis in preparation. Karlsruher Institut für Technologie (KIT), 2015.

[65] Susanne Mertens. "Study of Background Processes in the Electrostatic Spectrometers of the KATRIN experiment". PhD thesis. Karlsruher Institut für Technologie (KIT), 2012. URL: `http://digbib.ubka.uni-karlsruhe.de/volltexte/1000027058`.

[66] Benjamin Leiber. "Investigations of background due to secondary electron emission in the KATRIN-experiment". PhD thesis. Karlsruher Institut für Technologie (KIT), 2014. URL: `http://nbn-resolving.org/urn:nbn:de:swb:90-424154`.

[67] Philipp Rovedo. "Muon induced secondary electrons at the KATRIN experiment". Diploma Thesis. Karlsruher Institut für Technologie (KIT), 2013.

[68] Jürgen Reichenbacher. "Untersuchung der optischen Eigenschaften großflächiger Plastikszintillatoren für den KARMEN-Upgrade". Diploma Thesis. Universität Karlsruhe (TH), 1998.

[69] Richard Rink. "Measurements and Simulations with the Extended KATRIN Muon Detector System". Master's Thesis. Karlsruher Institut für Technologie (KIT), 2014.

[70] Kengo Watase. 2013. URL: `http://www.hamamatsu.com/sp/hc/osh/osh_0103_004_figure3.jpg`.

[71] M.A. Howe et al. "Sudbury neutrino observatory neutral current detector acquisition software overview". In: *IEEE Transactions on Nuclear Science* 51.3 (2004), pp. 878–883. DOI: `10.1109/TNS.2004.829527`.

[72] W.D. Apel et al. "Kneelike structure in the spectrum of the heavy component of cosmic rays observed with KASCADE-Grande". In: *Phys.Rev.Lett.* 107 (2011), p. 171104. DOI: `10.1103/PhysRevLett.107.171104`. arXiv: `1107.5885 [astro-ph.HE]`.

[73] K.A. Olive et al. "Review of Particle Physics". In: *Chin.Phys.* C38 (2014), p. 090001. DOI: `10.1088/1674-1137/38/9/090001`.

[74] 2012. URL: `http://www.physics.utah.edu/spectrum/index.php/news/83-2012/126-university-awarded-1-million-by-keck-foundation-to-study-cosmic-rays`.

[75] O.C. Allkofer and H. Jokisch. "A survey on the recent measurements of the absolute vertical cosmic-ray muon flux at sea level". English. In: *Il Nuovo Cimento A Series 11* 15.3 (1973), pp. 371–389. ISSN: 0369-3546. DOI: `10.1007/BF02734678`. URL: `http://dx.doi.org/10.1007/BF02734678`.

[76] V. F. Hess. "Über Beobachtungen der durchdringenden Strahlung bei sieben Freiballonfahrten". In: *Physikalische Zeitschrift* 13 (Nov. 1912), pp. 1084–1091.

[77] H.O. Klages et al. "The KASCADE Experiment". In: *Nucl.Phys.Proc.Suppl.* 52B (1997), pp. 92–102. DOI: `10.1016/S0920-5632(96)00852-3`.

[78] J. Abraham et al. “Properties and performance of the prototype instrument for the Pierre Auger Observatory”. In: *Nucl.Instrum.Meth.* A523 (2004), pp. 50–95. DOI: 10.1016/j.nima.2003.12.012.

[79] Claus Grupen. *Astroparticle Physics*. Springer-Verlag, 2005. ISBN: 3-540-25312-2.

[80] T. Stanev. *High Energy Cosmic Rays*. Springer-Praxis Series in Astronomy and Astrophysics Series. Springer, 2004. ISBN: 9783540406532. URL: https://books.google.de/books?id=B5GbQgAACAAJ.

[81] D.L. Hall, M.L. Duldig, and J.E. Humble. “Analyses of sidereal and solar anisotropies in cosmic rays”. English. In: *Space Science Reviews* 78.3-4 (1996), pp. 401–442. ISSN: 0038-6308. DOI: 10.1007/BF00171926. URL: http://dx.doi.org/10.1007/BF00171926.

[82] A. Saftoiu et al. “Measurements of the cosmic muon flux with the WILLI detector as a source of informationabout solar events”. In: *Rom.Journ.Phys.* 56.5-6 (2010), pp. 664–672. URL: http://www.nipne.ro/rjp/2011_56_5-6/0664_0672.pdf.

[83] O.C. Allkofer. *Introduction to cosmic radiation*. K. Thiemig, 1975. ISBN: 3-521-06098-5.

[84] Fabian Harms. “Experimental Study of Background Sources in the KATRIN Main Spectrometer”. PhD thesis in preparation. Karlsruher Institut für Technologie (KIT), 2015.

[85] B. Efron and R.J. Tibshirani. *An Introduction to the Bootstrap*. Chapman & Hall/CRC Monographs on Statistics & Applied Probability. Taylor & Francis, 1994. ISBN: 9780412042317. URL: https://books.google.de/books?id=gLlpIUxRntoC.

Acknowledgement

An dieser Stelle möchte ich mich bei allen bedanken, die mich beim Entstehen dieser Arbeit unterstützt haben, insbesondere danke ich folgenden Personen:

- Prof. Dr. G. Drexlin dafür, dass ich meine Masterarbeit bei KATRIN schreiben durfte und dafür, dass er mich für dieses Thema begeistert hat.
- Prof. Dr. T. Müller dafür, dass er freundlicherweise das Korreferats übernommen hat.
- Dr. Florian Fränkle für eine ausgezeichnete Betreuung, das Korrekturlesen meiner Arbeit und viele aufschlussreiche Diskussionen.
- Martin Kohler vom Institut für Meteorologie und Klimaforschung dafür, dass er mich freundlicherweise mit Wetterdaten versorgt hat.
- Dr. Benjamin Leiber, für seine Hilfsbereitschaft und zahlreiche Anregungen, sowie ihm und Richard Rink für die angenehme und nette Zusammenarbeit.
- Allen Doktoranden, Postdocs, Technikern, Wissenschaftlichen Mitarbeitern, Masterstudenten und allen anderen die dazu beigetragen haben, dass die Weihnachtsmessung wie geplant und ohne größere Probleme stattfinden konnte und durchgelaufen ist.
- Prof. Dr. Sanshiro Enomoto für die Bereitstellung von Beans und die Beantwortung meiner Fragen zu selbigem.
- Fabian Harms für diverse Hilfestellungen mit KaLi und ROOT.
- Nikolaus Trost für stets schnelle Hilfe bei PC-Problemen jeglicher Art.
- Florian Müller für ein immer offenes Ohr, seine stets ansteckende gute Laune und für die Motivation vor allem zum Ende hin.
- Allen, die im Laufe des letzten Jahres Kuchen mitgebracht, Pizza bestellt und geholt oder für Kaffee-Nachschub gesorgt haben.
- Allen jungen Wissenschaftlern für die schöne Zeit während und außerhalb der Arbeitszeit.
- Der Mittagessen und Skat-Runde bei den Kollegen der kosmischen Strahlung, insbesondere Daniela Mockler, die mich immer herzlich aufgenommen haben, wenn bei mir mal wieder alle in der Mensa gegessen haben oder ich einfach Lust auf eine Runde Skat hatte.

- Patrick Hetzel für die Kekse.

Der größte Dank gilt allerdings meiner Familie, vor allem meinen Eltern, die mich während meines Studiums immer unterstützt haben wo sie konnten und immer an mich geglaubt haben und ganz besonders meinem Mann Christian, der wohl vor allem unter meiner Schreibphase leiden musste und mir immer wieder liebevoll die Nerven geglättet hat.